DESIGN, SIMULATION, COMMISSIONING AND TEST OF THE TERTIARY BEAM AT FERMILAB

A DISSERTATION
SUBMITTED TO THE POSTGRADUATE DEPARTMENT
OF PONTIFICIA UNIVERSIDAD CATÓLICA DEL PERÚ
IN PARTIAL FULFILLMENT OF THE REQUIREMENTS
FOR THE DEGREE OF MASTER IN PHYSICS

Carlos Eugenio Pérez Lara

January 2010

Abstract

The present work describes the design and first test of a new low-energy hadronic beam and beamline at Fermi National laboratory. This new beam is the product of an intense group work during my internship at Fermilab on 2008. My work was focused on the study and simulation of all the feasible variations of the beamline taking into account the characteristics of the existing high energy beam, the space constrains within the experimental hall and the requirements for this new beam. The first part of this document gives a summary of the final design of the beamline and the expected response of its elements based on complete montecarlo simulation. This design was due by August 2008, when the actual construction of the beamline elements began. By October 2008, the first part of the beamline was mounted on the experimental hall and MINERνA was able to test the successful production of particles with a beam of pions at 16 GeV. For the test, my work was focused on the data analysis and truths comparison. The second part of this document reports the main results of this test and its limitations in the characterization of tertiaries.

Preface

The Fermi National Laboratory (Fermilab) is one of the biggest particle physics laboratories in the world. Located in Illinois-USA, Fermilab runs more than forty experiments in the fields of accelerator, flavor and neutrino physics.

CDF and DZero are the leading experiments on flavor physics. They use the Tevatron to study collisions of $p\bar{p}$ at center of mass' energies up to $\sqrt{s} \approx 2$ TeV. From these collisions they can measure the production and decay of massive particles, measure the production of high energy particle jets and photons and search for evidence of physics beyond the standard model.

On the field of neutrino physics, MINOS uses a neutrino beam in a dynamic range from 3 GeV to 15 GeV energy on axis in order to study the parameters related to neutrino oscillations and their interaction with nuclei.

On the other hand, the Meson Test Facility provides hadrons with energies ranging from 2 GeV to 120 GeV. This beam is used for the calibration of detectors and is obtained as the products of the Main Injector beam on an aluminum target.

On 2008 I made an internship at Fermilab working in the MINERνA project. This new experiment is designed to explore the interaction of neutrinos with nuclei and will provide measurements of the cross section with high accuracy. My work was focused on the design and simulation of the new low energy hadron beam that MINERνA needs for its calibration.

The present work will describe the design and analysis for the construction of the low-energy (300 MeV - 1.5 GeV) hadron beam. This beam requires also the versatility to select and bend a specific momentum as well as to provide particle identification. The momentum selection will be achieved by a particle-spectrometer and the identification will be complemented by a time of flight system. It is important to stress that after the installation of this beam Fermilab will be the only laboratory in the world that has such a tool for testing detectors.

In chapter 1, I briefly discuss the physics of the particle detectors used here

with some detail. The physics of these detectors by itself constitutes material enough for a many-page and technical review, that is why only the more important topics are examined, however I point out basic references where to an enthusiastic reader can be remitted.

Chapter 2 provides a description of the MINERνA experiment as well as a brief discussion on the interactions of neutrinos with matter that are important for the experiment. Again only a big overview of the experiment goals and its detector technology is given here giving the specific references for more details.

The design of the *Tertiary Beam* is exhaustively reported in chapter 3. This chapter starts with a rough overview of Fermilab's accelerator and the *Meson Beam*. Then it introduces the reader into the aspects considered for the design of the new beam with special attention in production, transport and reconstruction.

Chapter 4 reports the outcome of the first test we made to the beamline on November 2008. The beamline was not fully constructed and only studies on the particles' time of flight could be possible. The variety of tests that were made, the way we triggered and the MC gave us a first view of the species content and momenta predicted on chapter 3. However a verification of this result and a proper characterization of the spectrometer's arm has to be performed in future tests.

Finally, in chapter 5, I summarize the achievements so far and give an overall view of the status of its construction and future tests. Once finished, the *Tertiary Beam* can be used for experiments beyond MINERνA as its unique characteristics made it the first low energy hadron test beam.

Acknowledgments

I would like to express my sincere gratitude to my supervisor Alberto Gago for introducing me to the fascinating world of particle physics and whose encouragement and support from the beginning enabled me to develop an understanding of the subject. I am also heartily grateful to my other university teachers who forged my physical "sixth sense": Miguel Piaggio, Carlos Pizarro, Francisco Pasquel, Eduardo Massoni, Francisco de Zela, Hugo Medina, Rafael Coello and María Elena López. It is impossible to recall undergraduate times without remembering the old physics group: Marco, Laura, Pepe, Edith and David. In their company, I discovered the wonders of physics and enjoyed the interesting discussions at the faculty' students hall.

I am very grateful to the MINERνA group specially to Richard Gran, for teaching me so much about experimental physics; to Doug Jansen, for the insightful afternoon discussions and for breaking the monotony of my internship; to Jorge Morfin, for all the physics he taught me at those unforeseen meetings we had in spite of his busy agenda and for offering me his friendship; to Heidi Schellman, who made possible those long trips to the Northwestern University where I delighted attend some QFT lectures and for all her support; to David Boehnlein, for the physics discussions and for his inspirational personality. Furthermore I want to thank to the MINERVνA students of the summer of 2008: Aaron, Arturo, Ben, Brandon, Carmen, Cesar, Cody, Diana, Douglas, Emily, Jeawon, Jennifer, Jesse, Jorge, Kenyi, Lee, Melanie and Volodymyr without whom the internship would not have been so fascinating.

I owe my deepest gratitude to Gerardo Herrera for his invaluable academical advising through all these many years, for making me see beyond evident not only on academical matters but on life pursues and for honoring me with his friendship.

Although they would say "you don't need to do that", I would like to say that

I owe my loving thanks to my parents Eugenio and Betty whom set my moral values and ethics.

Finally, I would like to thank DAI-PUCP, the MINERνA experiment and the US Department of Energy which provide the financial support for this work.

to my beloved siblings: Angélica, Karina, Luis and Katya.

Contents

List of Figures

Chapter 1

The physics of particle detectors

In order to understand the physics of the particle detectors we need an adequate knowledge of the interaction of particles with matter. Fundamentally, when a particle goes trough matter, it interacts with its microscopic constituents and the specific interaction depends on both the inherent properties of the incoming particle (charge, mass, spin, flavor, etc.) and its energy. For instance, photons of a few hundreds KeV hitting a concrete wall primarily interact with the atomic electrons of the elements that compose the wall.

In the present chapter, I do not aim at giving an exhaustive treatment about the physics behind the interaction channels, but rather point out which are the main mechanisms leaving the details to the bibliography.

The scope of the present summary is for particles with $5 \times 10^{-2} < \beta\gamma < 10^{6}$, where β and γ are the usual kinematic parameters.

1.1 Energy loss of charged particles

Charged particles traversing matter lose energy mainly by excitation, ionization or showering. The *stopping power* is a useful quantity to describe the energy loss in a material and is defined as the average energy loss per length unit $\langle -dE/d\chi \rangle = \langle -dE/d(\rho x) \rangle$. Figure 1.1 shows the *stopping power* for μ^+ traversing copper as a function of $\beta\gamma$ and the leading process in each energy region.

Excitation and ionization region

A charged particle with a moderately relativistic energy will lose energy mainly by electromagnetic (EB) interaction with atomic electrons. For particles other

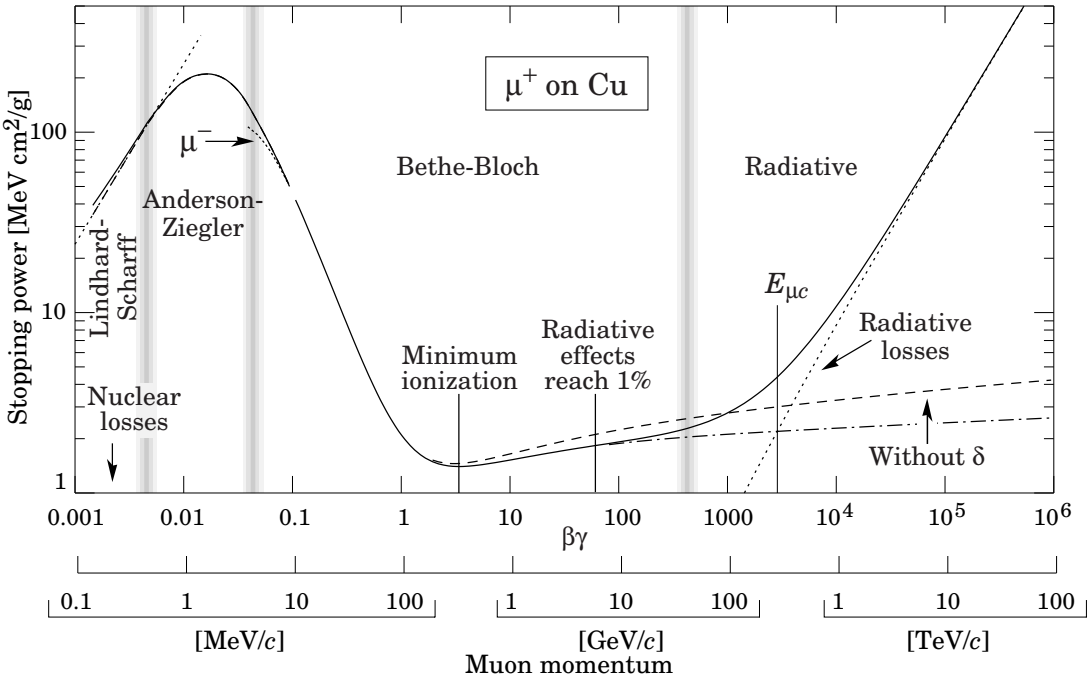

Figure 1.1: Stopping power for μ^+ going through copper as a function of momentum. Extracted from [1].

than electrons, we neglect the electron mass compared to that of the incident particle. In this scenario the mean energy loss is described by the ionization formalism of Bethe-Bloch [1]

$$\langle -dE/d\chi \rangle = K\frac{Z}{A}\frac{z^2}{\beta^2}[\frac{1}{2}\ln\frac{2m_ec^2\beta^2\gamma^2T_{max}}{I^2} - \beta^2 - \frac{\delta(\beta\gamma)}{2} - \frac{\zeta(I,\beta\gamma)}{Z}], \qquad (1.1)$$

where

K	$4\pi N_A r_e^2 m_e c^2 = 0.307075\,MeV cm^2 g^{-1}$
ze	Charge of incident particle
$Z(A)$	Atomic number (mass) of material
m_ec^2	Electron mass x c^2
I	Mean excitation energy $\approx 16Z^{0.9}eV, Z > 1$
T_{max}	$\frac{2m_ec^2\beta^2\gamma^2}{1+2\gamma m_e/M+(m_e/M)^2}$
$\delta(\beta\gamma)$	Density effect correction
$\zeta(\beta\gamma)$	Shell effect correction

T_{max} is the maximum kinetic energy transfer in a single collision, constrained

by the 4-momentum conservation $P_m^i + P_e^i \rightarrow P_m^f + P_e^f$. The derivation is straightforward and can be found in [2].

I, $\delta(\beta\gamma)$ y $\zeta(\beta\gamma)$ are modeled phenomenologically, see [3], [4] and [1].

The *mean excitation energy* I is associated to Bethe's perturbation model and in a semi-classical approach equals $\hbar\bar{\omega}$ ($\bar{\omega}$ being the mean atomic frequency of electrons). For practical purposes, the semi-empirical relation given by [5] is frequently used.

The *density effect* arises from the fact that the electric field is screened in the interaction with distant electrons. Due to Lorentz contraction, this reduces the logarithmic increase, see first term in equation 1.1, leading to a plateau behavior in the high energy regime. A general parameterization of this effect can be found in [5]. Figure 1.1 shows explicitly the importance of this correction.

The *shell correction*, on the other hand, deals with the opposite problem, that is the correction in the low energy regime, for the hypothesis of a stationary target does not meet at low momentum and the Bethe-Bloch's formalism collapses. The inclusion of this term allows to go down to $\beta\gamma \sim 0.13$ and provides a relative minimum at ionizing energies.

Other *low energy corrections* can be found in the literature given bellow.

The Bethe-Bloch equation is very useful in particle physics because most interactions of particles with detectors occur at these energy regimes. As equation 1.1 depends exclusively on β, this energy deposition is frequently used in low-momentum particle identification.

Electrons: When the mass of the incoming particle cannot be neglected, the ionization energy loss by collisions is better described by [3]

$$\langle -dE/d\chi \rangle = K\frac{Z}{A}\frac{1}{\beta^2}[\frac{1}{2}\ln\frac{\tau^2(\tau+2)}{2(I/m_ec^2)^2} + F(\beta,\tau) - \frac{\delta(\beta\gamma)}{2} - \frac{\zeta(I,\beta\gamma)}{Z}], \quad (1.2)$$

where τ is the kinetic energy of the particle in m_ec^2 units and the other parameters are the same as in equation 1.1.

$F(\beta,\tau)$ is a phenomenological expansion on τ that depends on the charge of the incoming particle. More information can be found in [1].

Radiative region

At high energies, particles slow down due to the EB field of the constituents of the atoms emitting photons. This deceleration is called Bremsstrahlung and it is

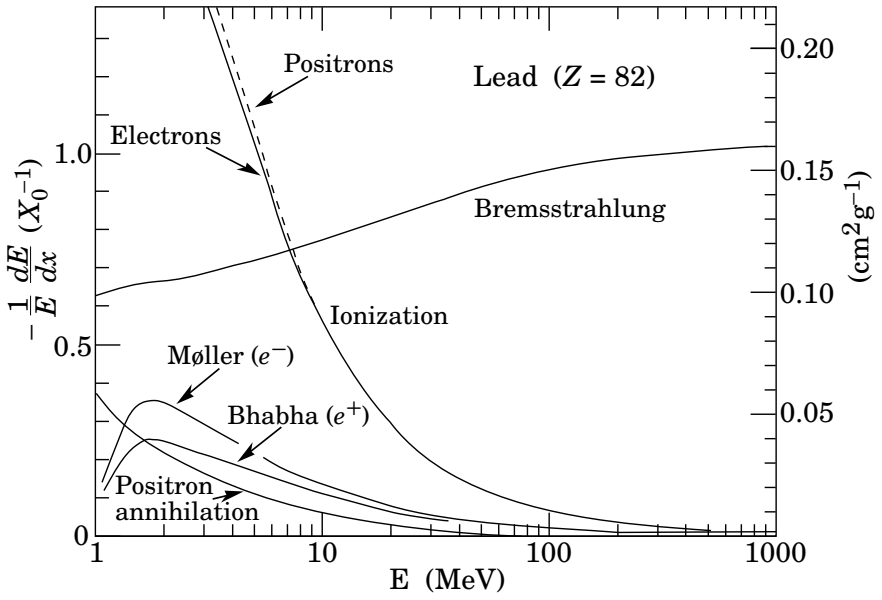

Figure 1.2: Fraction of energy lost by electrons and positrons as a function of energy. Extracted from [1].

the dominant channel at high energies where the EB field is stronger, see figure 1.2. Furthermore it is of particular importance for electrons as the cross section of the process is proportional to the inverse of the mass of the scattered particle.

Bremsstrahlung and pair production end in the development of electromagnetic showers. A phenomenon greatly used in calorimetry.

1.2 Interaction of photons

Photons interact with matter through any of the following channels:

Photoelectric effect

In the photoelectric effect, the photon loses energy in the ionization of the atomic electrons. This cross section increases dramatically when it reaches the ionization potential of every atomic shell (K, L, ...). This channel dominates at low energies, see figure 1.3.

Compton effect

Inelastic scattering dominates at medium energies, see figure 1.3. The incoming photon transfers part of it energy to the outer atomic electrons. A description

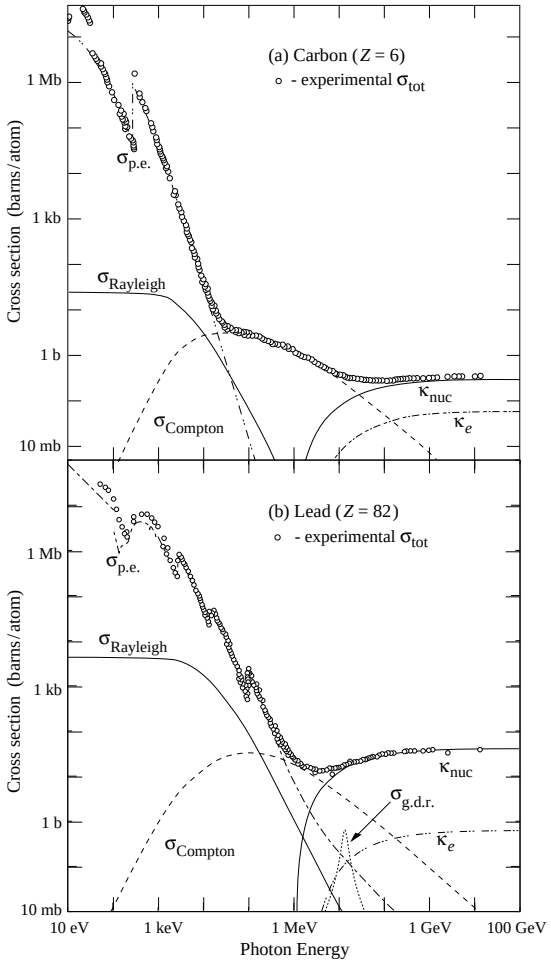

Figure 1.3: Cross sections for interactions channels of photons in matter. Extracted from [1].

of this effect was provided by A. Compton in the nineteen century and it is compacted in the Klein-Nishina formula [3] where we assume that the target electron is at rest.

Pair production

For energies larger than 1.2 MeV, the photon loses its energy mostly by $e^+ - e^-$ production. This umbral energy is imposed by the mass of the products, the more fundamental case being at $2\,m_e$. Due to invariance under Lorentz transformations, this process can only be possible in the electromagnetic field of either the atomic electrons or the nucleus. See [3] for further reference.

Chapter 2

The MINERνA experiment

The standard model describes the physics of all the fundamental particles known. The latter can be classified [6] according to the kind of interaction they take part on. On these lines, they can be grouped in two main categories: quarks and leptons, where only the quarks among all these fermions are subjected to the *strong force*. Among the leptons, the best known is the electron which is surrounding the nucleus in atoms and has been used intensively in applied science.

Table 2.1: Elementary particles in the standard model

Leptons			Quarks			Propagators		
e	μ	τ	u	c	t	γ	Z^0	g
ν_e	ν_μ	ν_τ	d	s	b	W^+	W^-	

Three of these leptons are called neutrinos (ν_e, ν_μ, ν_τ) due to their absence of charge and negligible mass. Neutrinos are of special importance in the understanding of the Universe, for they are the best candidates to study different models of the combustion in stars. Moreover, recent studies indicate that they might explain at least partially for the dark matter, which composes the greater part of the Universe.

Many studies of neutrino physics have been performed since neutrinos were discovered. A phenomenon called *Neutrino Oscillations* is a striking quantum-mechanical manifestation of the characteristics of the neutrino (weak interacting particle with nonzero mass). By understanding neutrino oscillations, we can correct the neutrino fluxes detected from far supernovas and improve the estimation of their distance from us.

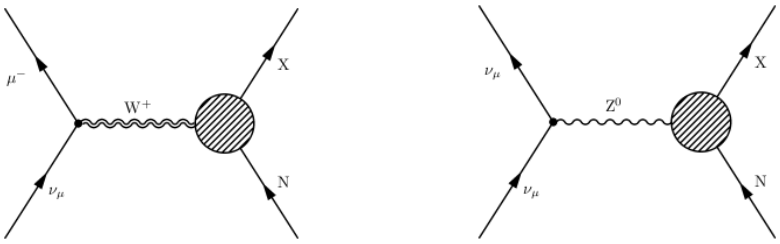

Figure 2.1: Neutrino scattering processes. Left: Charge current interaction. Right: Neutral current interaction. N, stands for nucleon, and X, for hadronic final states

Fermilab has a high intensity neutrino beam (NuMI Beam). This well understood beam is suitable to explore neutrino properties and is currently used by MINOS [6] in the pursue of measuring the disappearance of ν_μ. NOνA [7] will continue the efforts on neutrino oscillations in the future. MINERνA, on the other hand, will focus on neutrino interactions with nuclei and will provide to the neutrino community with precise measurements of the ν and $\bar{\nu}$ cross sections with Ca, Fe and Pb. These cross sections are specially important at low energies where a better characterization of the nuclear structure is needed. On these lines, the neutrinos can help to explore the structure of the nucleus as no other lepton can do, due to its exclusive axial component.

Before describing MINERνA, in the next section I comment briefly on the interaction channels of neutrinos with nucleus that are relevant in order to understand the physics of MINERνA.

2.1 Neutrino - nucleon scattering

The neutrino interacts with nucleons through charged and neutral current processes, see figure 2.1. The available channels in which it can interact depends on the capability of the incoming neutrino to resolve the nucleus. The most common channels will be presented in this section.

Quasi-elastic scattering

In Quasi-elastic (QEL) νN scattering the nucleon does not break into lighter hadrons. Processes of such nature are the following:

$$\nu_\mu + n \rightarrow \mu^- + p \quad \text{and} \quad \bar{\nu}_\mu + p \rightarrow \mu^+ + n \qquad \text{for CC interactions}$$

$$\nu_\mu + p \to \nu_\mu + p \quad \text{and} \quad \bar{\nu}_\mu + p \to \bar{\nu}_\mu + p \qquad \text{for NC interactions}$$

The formalism for describing such interactions is given by the V-A theory [8]. The most general matrix element for QEL interactions is $\frac{G_F}{\sqrt{2}} \times \bar{u}_\mu(p')\gamma_\alpha(1-\gamma_5)u_\nu(p) \times \langle p(P')|J^+_\alpha|n(P)\rangle$, where $\bar{u}_\mu$ and $\bar{u}_\nu$ are the leptonic spinors. The hadronic current is of the form

$$\langle p(P')|J^+_\alpha|n(P)\rangle = \cos\theta_C\, \bar{u}_p(P')\{\gamma_\alpha(F_V - F_A\gamma_5) + \frac{i\,\sigma_{\alpha\beta}\,q^\beta}{2M}F_M\}u_n(P).$$

While the nucleon form factors F_V and F_M can be obtained by elastic scattering of leptons as well, the axial form factor above $Q^2 > 100$ MeV^2 is only accessible with neutrinos. An extended discussion about these form factors as well as compelling evidence of its deviation from the usual dipole approximation can be found in [1] and [9].

Resonant pion production

Above $Q^2 > 1$ GeV^2 and below the parton-model regime, the hadronic final states are mostly due to resonant particle decay, typically $\Delta(1232)$ as in

$$\nu_\mu\, p \xrightarrow{\Delta^{++}} \mu^-\, p\, \pi^+ \qquad \nu_\mu\, n \xrightarrow{\Delta^{+}} \mu^-\, n\, \pi^+ \qquad \nu_\mu\, n \xrightarrow{\Delta^{+}} \mu^-\, p\, \pi^0$$

$$\nu_\mu\, p \xrightarrow{\Delta^{+}} \nu_\mu\, n\, \pi^+ \qquad \nu_\mu\, p \xrightarrow{\Delta^{+}} \nu_\mu\, p\, \pi^0 \qquad \nu_\mu\, n \xrightarrow{\Delta^{0}} \nu_\mu\, n\, \pi^0 \qquad \nu_\mu\, n \xrightarrow{\Delta^{0}} \nu_\mu\, p\, \pi^-$$

However, as the theoretical model [9] for this reactions is not as simple as in the previous case, the form factors differs from QEL and more data is needed to properly describe the total cross section at these energies.

Coherent pion production

For more than 30 years it has been well known that the week interaction violates parity. In electromagnetic terms this comes from an interference of vector and axial vector couplings. Coherent production of π^0 for neutrino neutral current interactions at low Q^2 and small angles evinces the V-A structure of neutrinos.

The main reaction is $\nu + (A, Z) \to \nu + \pi^0 + (A, Z)$ which leaves the nucleus unaltered. Event though this process is highly contaminated by other sources of pion production, its recognizable kinematic signature allows its identification. For the helicy conservation in the process, the π^0 distribution peaks at the forward direction.

The quark-parton model

The double differential cross section for CC ν-p interaction is
$$\frac{d\sigma^{\nu,\bar{\nu}}}{dx\,dy} = \frac{G_F^2}{2\pi(1+\frac{Q^2}{m_W^2})^2}(xy^2\frac{M}{\nu}W_1(x,y)+(1-y-\frac{Mxy}{2E}W_2(x,y)\pm xy(1-\frac{y}{2}W_3(x,y)))),$$
where: $\nu = E_\nu - E'_\mu$ is the energy transfer in the laboratory frame, $x = \frac{Q^2}{2M\nu}$ is the usual Bjorken scaling variable, and $y = \frac{Q^2}{2MEx}$ is the inelasticity. The three W functions model the effective protons structure that sees the neutrino.

It is well known now that nucleons indeed have a structure of valence quarks which interact in a non-conspicuous way. These interactions which are strong at low energies encapsulate the spatial extension of the target into form factors $F(Q^2)$. These factors could also be understood as a fourier transform of the spatial charge of the target [8]. Due to the asymptotic freedom the underlying structure of nucleons manifests itself as energy increases, $Q^2 > 2$ GeV^2, and the form factors become independent of Q^2.[1] The scattering process at this level resembles that of a point-like target and the scaling invariance allows us to describe the interaction as an incoherent hard elastic scattering, also know as Deep Inelastic Scattering (DIS), followed by fragmentation and hadronization processes [1].

Thus, on first order approximation, at high energies the parton distribution functions only depend on one variable:
$$MW_1(Q^2,\nu) = F_1(x) \qquad \nu W_2(Q^2,\nu) = F_2(x) \qquad \nu W_3(Q^2,\nu) = F_3(x)$$
and measurements on the scattering cross section allow us to explore the behavior of these functions.

Nuclear effects in neutrino interactions

Measurements of $F_2(x)$ for various different nuclei reveal a suppression for high Z nuclei. The reduction responds to two different effects because of the two different dominant quarks nature at those extremes. At low x the coherent interference gives rise to a phenomenon called shadowing, while at high x the scattering can be treated as an incoherent reaction from bound nucleons parametrized by phenomenological models.

[1] However, as the energy increases we recover the dependency on Q^2 but due to a different phenomenon. This is deeply discussed on [1].

Much effort has been done on this area, but we are still far from a clear understanding of the phenomena involving nuclear effects. A phenomenological approach by the time being could be more reveling than actual lattice QCD calculations. See [10] for further details.

2.2 The MINERνA experiment

The **M**ain **IN**jector **E**xpe**R**iment ν - **A** (MINERνA) is a high-statistics neutrino scattering experiment that will run in the NuMI Beam Hall at Fermilab. The experiment will use an intense and well-understood ν beam and a fine-grained detector to collect a large sample of ν and $\bar{\nu}$ scattering events. The detector is a combination of a fully active detector at the core surrounded by a traditional calorimeter and will be placed just upstream the MINOS near detector about 100 m below surface.

It will run for four years in total. The first year it will run in parallel with MINOS with a low-energy neutrino beam peaking at 3 GeV. The rest of its running life will be in parallel with NOνA subjected to a medium-energy beam peaking at 7 GeV.

2.2.1 Goals

The aim of MINERνA is to measure with high precision the cross section of ν-A interaction in

- the QEL-low x region: at both low and high Q^2 the active detector allows identification of small recoils and prompt showers;
- the resonance-dominated region: the detector allows a good reconstruction of the angular distributions and invariant mass;
- the coherent single pion production region: the fiducial volume allows a clear reconstruction of the low angle pions;
- nuclear-effect-dominated region: for there is evidence that shadowing with neutrinos differs from that with charged leptons, MINERνA will explore that region and also the high x region to test the current models;

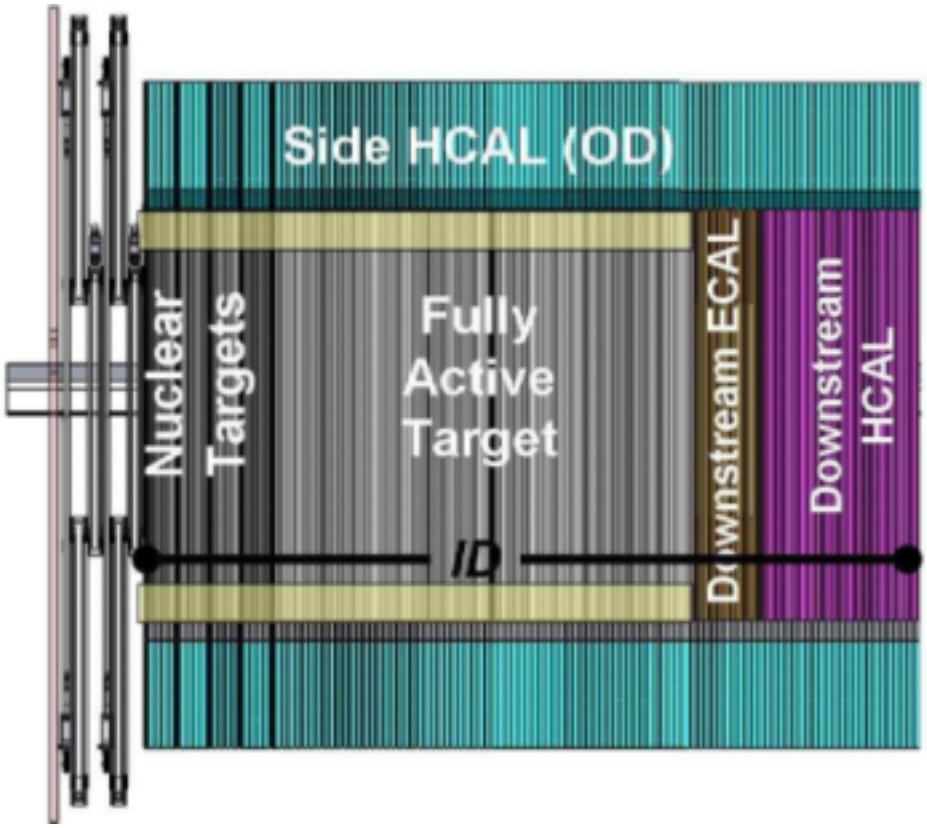

Figure 2.2: Schematic side view of the MINERνA Main Detector.

- DIS: specially at high x MINERνA will improve the parton distribution functions;

Moreover many other investigations will be made with MINERνA such as the study of the transition from resonance to DIS, the examination of the leading exponential contributions of perturbative quantum chromodynamics, the measurements of V_{us} and V_{cd}. A complete list of the possibilities with MINERνA can be found in [9].

2.2.2 The main detector

The complete detector is $3.5 \times 4 \times 4.6$ m^3 and weights 300 tons. It is divided by its use in two parts: the inner detector, which consists of set of hexagonal planes; and the outter detector, which surrounds the six borders of the ID.

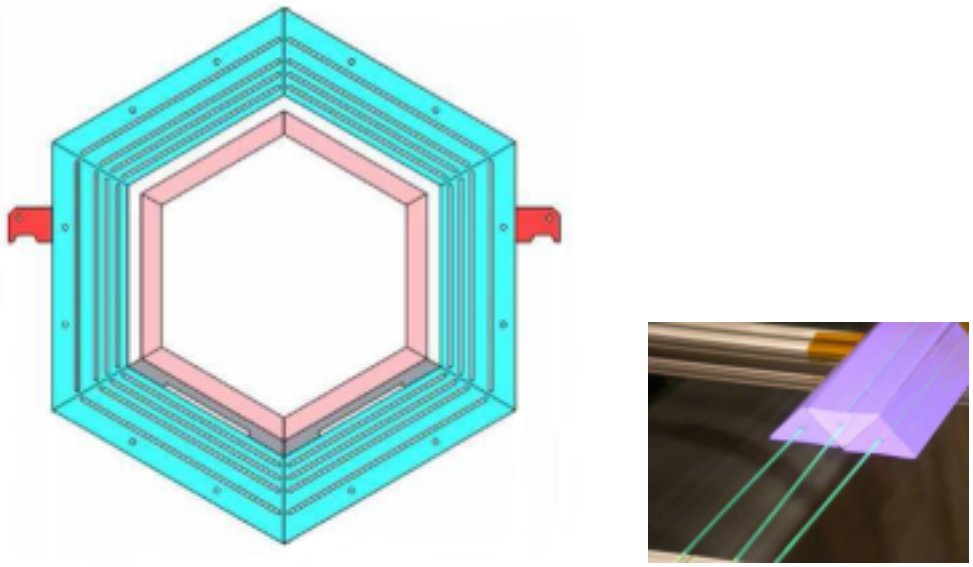

Figure 2.3: Fiducial volume of the MINERνA detector. Left: drawing of a standard plane of the fiducial volume showing also the OD. Right: a photo of scintillator bars showing the central extrusion and WLS fibers.

The inner detector (ID)

Each hexagonal plane in the detector is an array of coated scintillating bars of triangular cross section (1.7 cm height with 3.3 cm base) which gives MINERνA's high tracking capabilities. These bars are extruded so that a wavelegth shifter (WLS) fiber runs in the middle. The scintilator has a core of polyestirene doped with a florescent blue light emitor and the WLS fibers are couple directly to photomultiplier tube to avoid unnecessary loses.

In order to have a 3D reconstruction of the trajectories, a rotation of 60° among planes is used. Two of these planes are grouped in one module, which can be X-U or X-V according to their relative position.

An electromagnetic calorimeter (ECal) is placed downstream the fiducial volume. The ECal has 20 special modules with a combination of 2 mm Pb and a regular scintillating plane. This systems will be able to contain showers made by photons with an energy of a few GeVs.

An hadronic calorimeter (HCal), with also 20 layers, is placed downstream the ECal. This time the scintillating plane is next to a one inch Fe plane which, even though it degrades resolution, allows to fully capture muons below 600 MeV. For high energy muons and protons the MINOS near detector will complete the track.

The first 14 modules of the ID contains the nuclear targets in a very peculiar arrangement. MINERνA will study interactions with carbon, iron and lead. The configuration of these modules is as follows:
$U - [Pb/Fe]_1 - UV - [Pb/Fe]_2 - UV - [Pb/Fe/C]_3 - UV - [Pb]_4 - UV - [Pb/Fe]_5$.

The modules $[Pb/Fe]_1$ and $[Pb/Fe]_2$ will contained a plane of 60% Fe and 40% Pb rotated from one each other in order to check differences in the detection. The module $[Pb/Fe/C]_3$ will be 50% C, 30% Fe and 20% Pb. These three first modules will have a thickness of 2.5 cm. The module $[Pb]_4$ will have a thickness of 0.75 cm which will trigger the photons shower. The module $[Pb/Fe]_5$ will have the same composition than the first one but with only 1.25 cm of thickness and will produce interactions mainly for the low energy spectra allowing the fiducial volume to measure multiplicity.

The outer detector (OD)

Each one of the ID planes will be extended out of the active detector so that an electromagnetic and hadronic calorimeters will be mounted on the outer region. This arrange is called the outer detector and will surround all the ID in six readout-independent blocks. For the ECal, rectangular scintillator bars ($1.9 \times 1.5 cm^2$) with the same extrusion that those in the ID will alternate with 2 mm Pb trapezoidal sheets. On the other hand, for the HCal five gradually increasing trapezoidal Fe blocks summing up to 43.4 cm of thickness will be separated by four 2.5 cm scintillating bars similar to those in the ECal. This design allows the completely containment of photons entering the OD and high resolution reconstruction for those at angles below 25°. Its large mass also allows the fully stop of protons up to 750 MeV entering at right angles.

2.2.3 The TestBeam detector

The response of the active volume of the detector to the passing of hadrons must be calibrated beforehand. For this purpose, a exposure of the fiducial volume as well as the electromagnetic and hadronic calorimeters to an hadron test beam will take place at the Meson Test Facility at Fermilab. Due to the large volume and complexity of the main detector, the MINERνA experiment is building another detector with all the same characteristics of the main detector but smaller in volume.

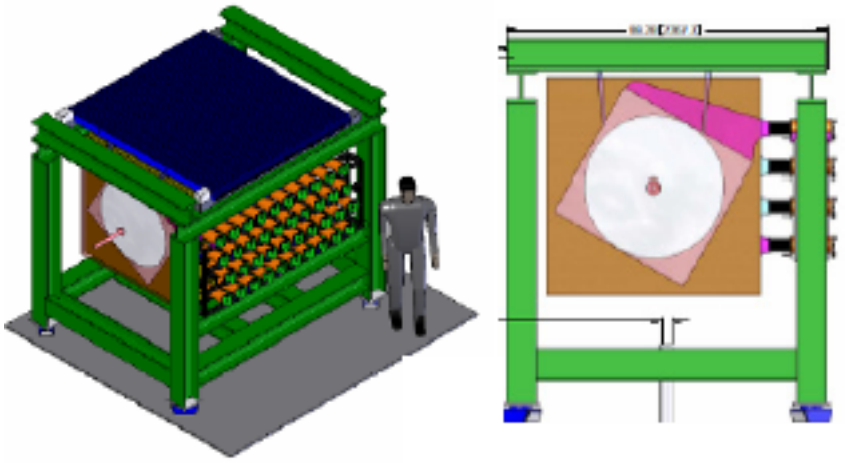

Figure 2.4: MINERνA TestBeam detector

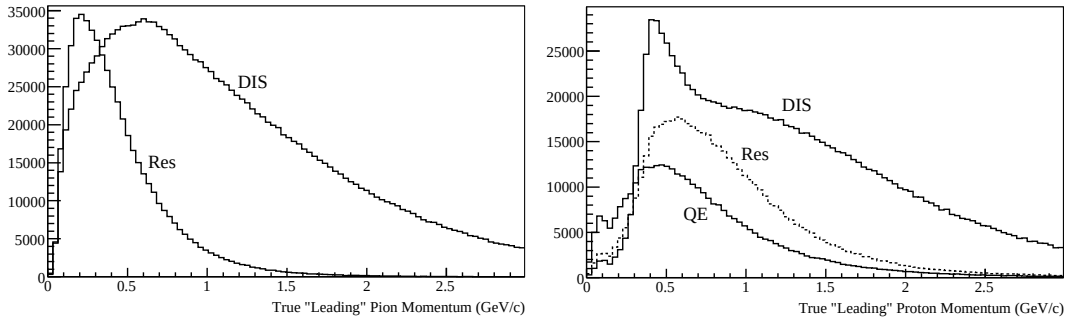

Figure 2.5: Pions and protons expected. MC Simulation using NeuGen provided by R. Gran.

The TestBeam detector will measure the response of the fiducial volume and the data adquisition (DAQ) system when hadrons of the energy expected by a neutrino interaction travels through the detector. The detector is 1×1 m^2 and will consist of 40 modules with removable Fe and Pb modules using the same characteristics of the ID. It has a complex running plan in which the configuration of the modules per run will vary according to the specific test needed.

Montecarlo simulation in NUEGEN by Richard Grand points out that the hadrons energy distribution coming from QEL, resonance and DIS should peak at about 0.5 GeV for pions and protons; see figure 2.5. So an update of the existing test beam facility at Fermilab is needed to reach those energies. The Tertiary Beam that is currently being constructed will meet those requirements. The design and characteristics of this test beam are presented in the next chapter.

Chapter 3

Conceptual design of the tertiary beam

The source of the beam used in all the experiments at Fermilab is ionized hydrogen H^- [11]. A Walton-Cockcroft multiplier [12] generates the field in which the hydrogen negative ions are accelerated until they reach a kinetic energy of 750 eV. This pre-accelerated beam is transfered to a *Linear Accelerator* (LINAC) in which it reaches 400 MeV. The acceleration is made by a series of RF-cavities [12] that also shape out the time structure of the beam.

At the end of the LINAC, the H^- beam bunches are injected into a small synchrotron (*Booster*) where the electrons are striped off from the hydrogen ions [13] and the remaining protons are accelerated up to an energy of 8 GeV. The *Booster* design allows 84 bunches per rotation (batch) and the transit time when rotating at full speed is 1.6 μs. That is, the bunches are separated by about 19 ns.

Once the protons reach 8 GeV, they are transfered into the *Main Injector* (MI), a seven times bigger synchrotron. The batch injection can be set up so that more than one booster-batch is transfered to the MI. This is specially useful for intensity requirements by the fixed target experiments. The MI allows 7 booster-batches per rotation. Once the injection is finished the whole batch is accelerated to energies up to 150 GeV with a transit time of 11 μs. The MI, besides its accelerating features, acts as a beam distributor. It manages the production and recycling of $\bar{p}$, the injection of p and $\bar{p}$ to the *Tevatron* and the beam delivery to the *Switchyard*. The latter distributes 120 GeV protons to two current beamlines: The *NuMI Beamline* and the *Meson Beamline*.

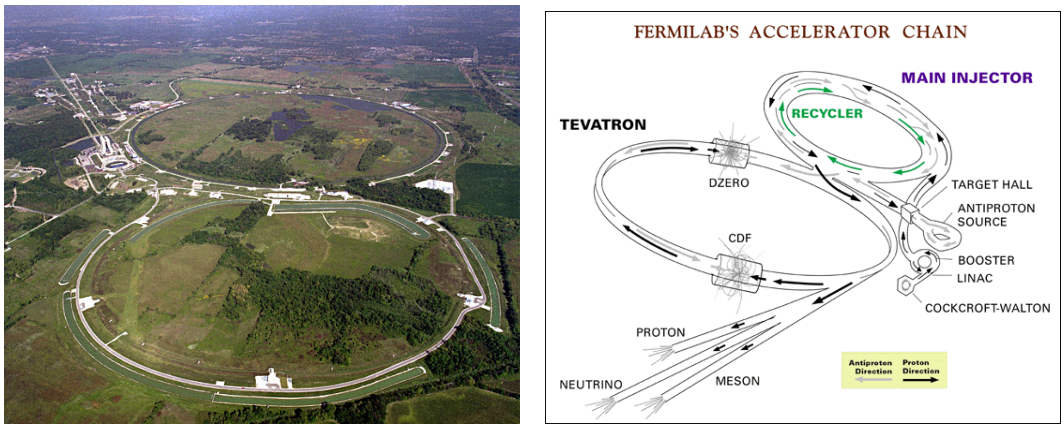

(a) Aerial view of the accelerator rings (b) Fermilab's accelerator chain

Figure 3.1: Fermilab's accelerator chain. The ions are accelerated in the LINAC, Booster and MI. The MI supplies beam to the Tevatron, the NuMI and the Meson Test. Courtesy of DOE.

The *NuMI Beam* is generated by the decay of mesons produced in the NuMI target [6]. It has the larger baseline at the laboratory (about 735 km) and is used to study neutrino oscillations and neutrino interactions. MINOS [6] uses this baseline to measure the parameters governing flavor oscillations, while MINERνA [9] and NOνA [7], currently being constructed, will complement the studies by measuring the cross sections of neutrino interactions with nuclei. More information about these experiments can be found in the bibliography.

The *Meson Beam* is made by the momentum selection of products from 120 GeV protons on an aluminum target. There are five places where this beam can be delivered. One of them is the *Meson Test Hall* (MTest), where many experiments around the world can study the response of their detectors to a mono energetic hadron beam.

The new low energy hadron beam (*Tertiary Beam*), tuned for production at energies at the range of hundreds of MeVs, will be placed in the MTest. The design of this new beam, which is the product of my internship at Fermilab and subject of the present thesis work, will be described in section 3.2, but before that I will point out the main characteristics of it source: The *Meson Beam*.

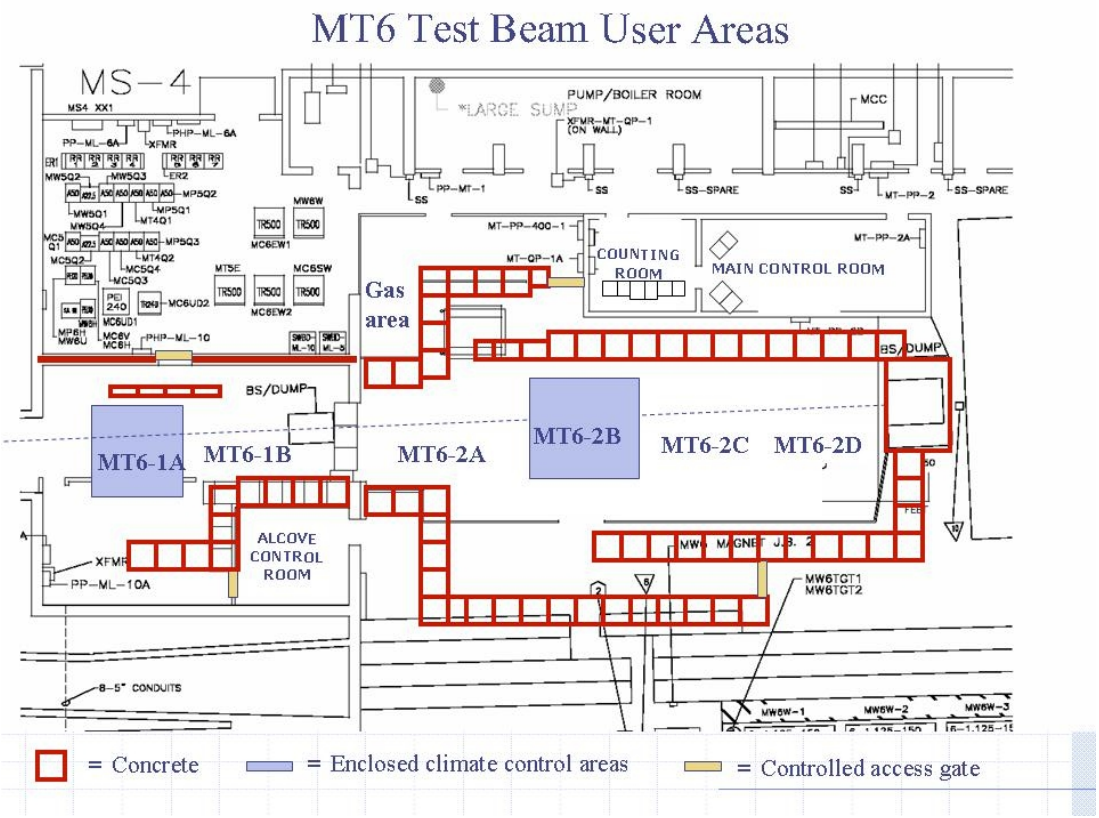

Figure 3.2: Meson Test hall at Fermilab showing the six experimental available areas: MT6-1A, MT6-1B, MT6-2A, MT6-2B, MT6-2C and MT6-2D

3.1 The Meson Beam

The Meson Beam results from the collision of 120 GeV protons on a 12" aluminum target. The products are directed towards the MTest in two modes of operation: In *proton mode*, the noninteracting proton beam is mostly absorbed by a pinhole collimator and the remaining beam is transported directly to the MTest; while in *pion mode*, the selection of different momenta is made by the use of dipole magnets along the beamline. This last mode can provide pions with energies as low as 1 GeV. Below that energy almost all the content of the beam is e^+ - e^- coming from showering or decays.

Under normal conditions, the MI duty cycle is 3/60 and it can deliver beam for 12 hours a day. The current operation mode extracts only one particle per MI-rotation, that is 90kHz, in a slow process called resonant extraction [12]. At this mode a nominal spill is composed of about 270k particles. However, as it was discussed above, one can select different intensities by multiple batch injections.

It has been reported in [14] that the probability of double occupancy per

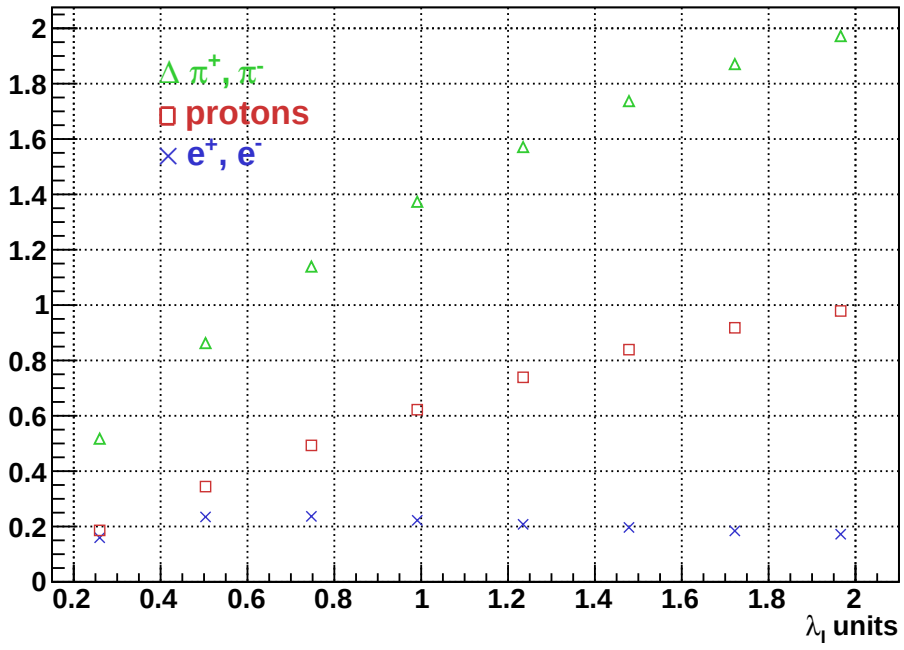

Figure 3.3: Multiplicity of particles produced per pion on target for different target lengths. Triangles stand for pions; squares, for protons, and crosses for electrons and positrons.

bunch can be up to 35% due to the resonance extraction. Even tough this fact could be an issue for detectors working on the secondary beam, this probability is highly reduced for the Tertiary Beam as it will be discussed below.

3.2 The Tertiary Beam

The Tertiary Beam must meet the following characteristics:

1. to provide e^+ - e^-, pions and protons with momentum within 300 MeV/c and 1500 MeV/c;

2. to have a good balance in the event rate, so that even a slow DAQ, as MINERνA's, can process the signal;

3. to inform to the DAQ the characteristics of the specific particle that is triggering.

A slow mixed beam was designed to meet all this requirements. The tertiaries are produced by a copper target and selected with a momentum spectrometer. A

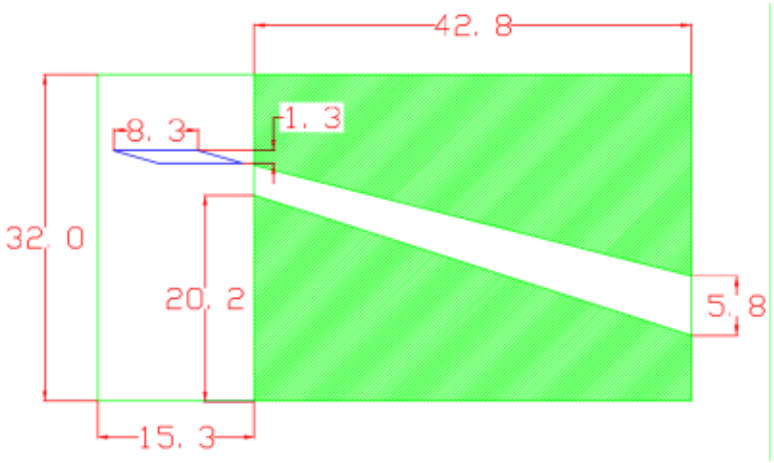

Figure 3.4: Target and collimator design. Trapezoidal copper target hooked to a steel dumper-collimator. The dimensions are in inches.

Time of Flight (TOF) system was also included to complete the particle identification. This setup was finalized and reported by August 2008 [15]. The tertiary beamline has to be as short as possible in order to suppress pion decay and assure a high intensity. That is why the target and the collimator were placed at MT6-2A, see drawing 3.2, so the characterized beam is available at the last three user areas. MINERνA will locate its TestBeam detector at MT6-2B to gain the highest pion intensity possible.

3.2.1 Production of tertiaries

When the secondary beam hits the target, besides the production of tertiaries, the remaining secondaries propagate also in the Hall. Even though the secondaries and tertiaries are not on time, so it is possible to separate both signals at level zero, the secondary beam is absorbed in order to keep the radiation level low. In this way a sensitive device in the detector chain is not exposed to an unnecessary contamination.

A compromise among the size of the target, dumper and the intensity - energy of the secondary beam exists and was taken into account for the beamline design.

The intensity and diversity of tertiaries depends on the characteristics of the secondary beam. Copper was chosen as the target due to its compactness and low activity.

Regarding the variety of species, the production of energetic e^+ e^- pairs comes by electromagnetic cascade of a prompted gamma ray or by π^0 decay.

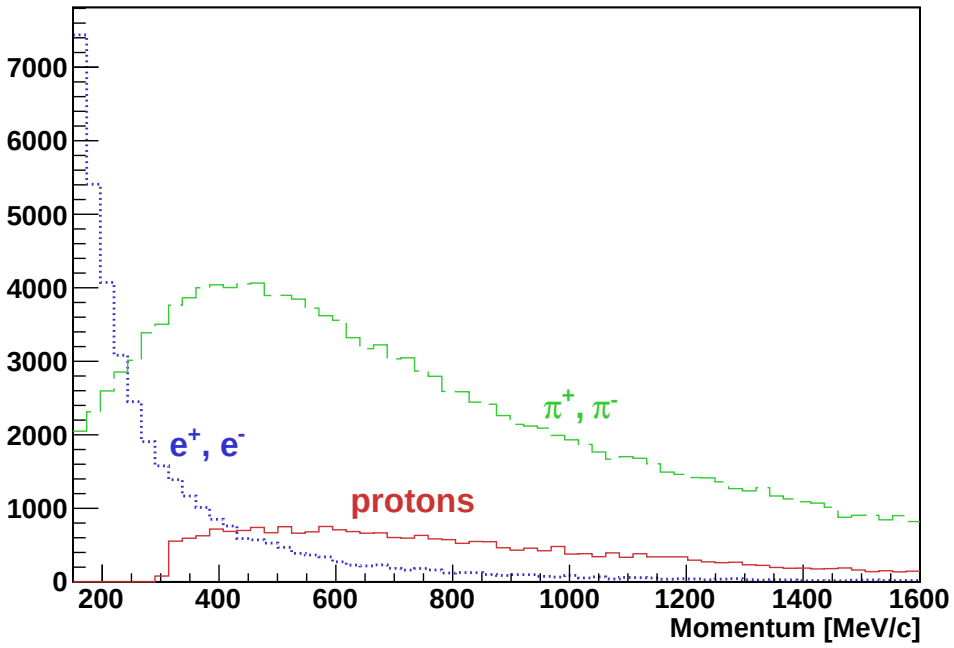

Figure 3.5: Expected rate and species of particles comming out from the end of the collimator for 15 M pion on target.

The π and proton production comes from the excitation of nucleus. A phenomenological model called Binary Intra nuclear Cascade (BIC) is used by geant4 [16] between 200 MeV and 10 GeV. Inelastic scattering leads to excited nucleus which decay in turn by fission or other pre-equilibrium emissions. The daughters themselves may interact again developing a nuclear cascade that finishes when the energy falls down bellow a model-dependent tunable threshold. I used g4beamline [17], a geant4-based programed tailored for beamlines, to analyze the production of tertiaries and the levels of radiation expected.

Figure 3.3 shows the length dependence on the production of species for a copper cylindrical target exposed to a 16 GeV pion beam. Notice how the compromise between production and absorption manifest itself by a reduction in the slope as the target enlarges. This effect is clearer for electrons and positrons where a local maximum is obtain at about $0.6\lambda_I$ ($\chi_0 = 9.37\%\lambda_I$). From this analysis a $1.4\lambda_I$ target is suitable for the beam required, that is a 8.3" copper target.

It has been reported [1] that the interaction cross section for pions on nucleus as the energy ramps down from 16 GeV until 300 MeV increases by a factor of 5 for

Counter	Fluence Neutrons (cm^{-2}/spill)	Dose (prem/spill)
A	132.9	385.0
A´	9.6	65.2
B	36.8	57.5
B´	2.3	15.6

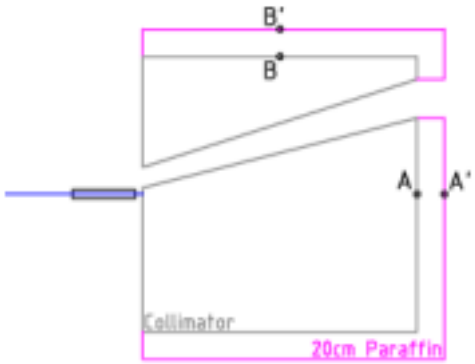

Figure 3.6: Neutron dosis at beamline. A 20cm paraffin wall surrounding the dumper was implemented. Fluences and equivalent doses are shown in the upper table.

π^+ and by a factor of 3 for π^-, see [1]. In order to reduce the loss of low energy particles due to multiple interaction, we stretch the path that tertiaries travel without reducing the target size. This is accomplished by designing a trapezoidal target [18] and extracting tertiaries at a fixed high angle as it is shown in figure 3.4. With this design we can expect that most of the hadrons extracted comes from a first generation (tertiaries).

Angular selection of tertiaries

Once the particles are being selected through the collimator, they are bended back to the hall. The spectrometer was chosen as the returner in order to minimize the tertiary baseline. This spectrometer has a couple of $0.34\,T$ magnets previously used in the *debuncher* [13]. Considering the bending power and the space constrains imposed by the hall, we selected particles coming at 16° from the target and placed a steel dumper with a wide channel to allow the collimation of the beam.

Figure 3.5 shows the spectrum of particles expected at the end of the collimator's channel for a 16 GeV pion beam on target. The Monte-Carlo predicts that the leading specie is pions peaking at 450 MeV. Protons are also produced but

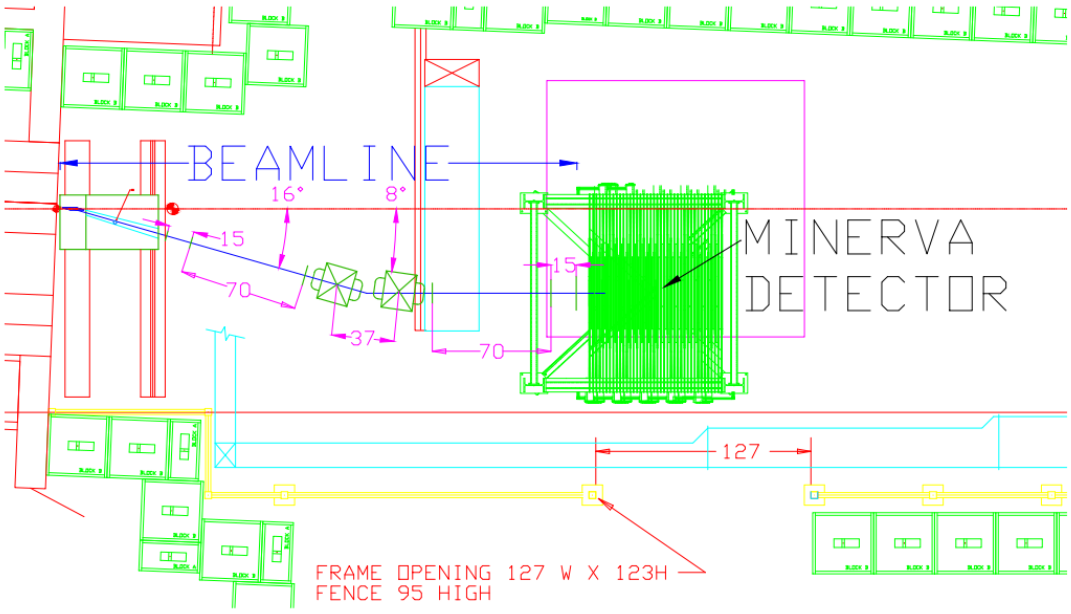

Figure 3.7: Tertiary Beamline and the MINERνA TestBeam detector inside the experimental hall

its population is only one fifth of that of pions. Below 400 MeV the population of electrons and protons are the same. Below 200 MeV most of the beam is electrons and positrons. However due to the geometry and the trigger design very few, if any, of these particles will fire. This feature will be discussed in the next section.

Furthermore MC studies on neutron doses and actual measurements point out that the level of neutrons produced is so low that it does not penetrate the MTest concrete shielding and does not present bio-hazards for an operator near the experimental hall. The MC prediction for thermal neutrons reaches up to 25 nrem/hour dosis on point A, see figure 3.6. This dose is very low for any accidental human exposure to the beam [19]. Moreover most of the neutrons coming from the collimator are slow and according to MC only 20 cm of paraffin reduces the rate by a factor of 6.

The target and collimator were tested at MT6-2A on October 2008. The results of the evaluation is extensively discussed on the next chapter.

3.2.2 The beamline

The beam coming out from the collimator contains many species and momenta. Hence the elements of the beamline that follows the collimator need to bend the

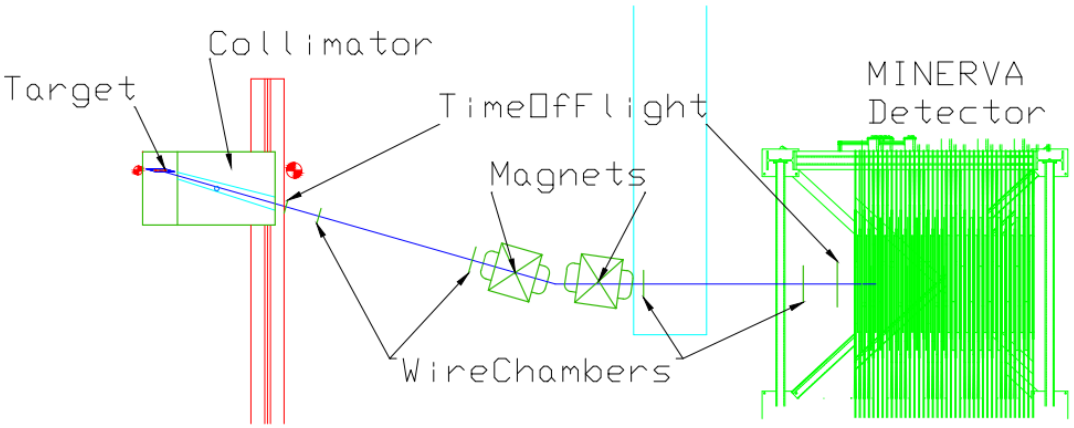

Figure 3.8: Tertiary Beamline details showing the spectrometer elements and baseline

beam back and allow the user to trigger on an specific particle specie and momentum. This is accomplished by placing a dipole magnet system, for momentum selection, and a time of flight system, for particle identification.

The list of the elements of the beamline includes: A steel collimator with a channel of increasing width; two dipole magnets, with a wide window acceptance; four wire chambers, two before the magnetic bend and two after; and two scintillator counters, at the ends of the spectrometer. A drawing of the MTest experimental hall with the location of the beamline elements is shown in figure 3.7 and 3.8.

The magnets

Among the magnets available at Fermilab, a couple of air-cooled dipole magnets were chosen. These magnets were used in the *debuncher* long ago and have an aperture of about 30 cm by 15 cm, see picture 3.9.

MC simulation performed by D. Jensen, fnal points out that each one of these magnets can develop a reproducible steady field of 3.4 kG, 100 Amperes, for a long period without overheating. A description of the magnet -coils and yokes- was supplied to Superfish [18] to check the temperature at magnets versus running time, see figure figure 3.10. These values were later confirmed by an actual measurement in the hall, see figure 3.11.

On the other hand, even though a complete mapping of the magnetic field will be perform later, Superfish indicates that about 90% of the window has an

Figure 3.9: One of the dipole magnets that will be used on the beamline.

evenly distributed magnetic field. That is why, for the present work, I assume a completely even magnetic field inside the window for MC purposes. This will give us a good reference of the bending.

Figure 3.11, from the ACNET monitor [20], shows the secondary beam yield and the current at the magnet for seven spills. Note that the magnet is only powered while there is beam in the hall, that is 3 seconds every minute. Hence for 100 Amperes the magnet behaves below saturation and generates a reproducible field. In the following analysis, the implementation of the main yoke and an approximation of the expected fringe fields has been supplied to g4beamline, see 3.12.

The wire chambers and the spectrometer resolution

The wire chambers of the HyperCP experiment [21] are used as trackers. These chambers are formed by four planes (XUVX') with 1 mm of wire pitch. The vertical wires at X and X' are offset by 0.5 mm and the U-V planes form an angle of $\pm \tan^{-1}(1/2)$ with the vertical. Thus a stereo resolution of 0.5 mm can be reached without the need of drift time reconstruction. This allows the chambers to be close to the dipoles without compromising the resolution.

The readout system is being developed at Lab6 - Fermilab by MINERνA

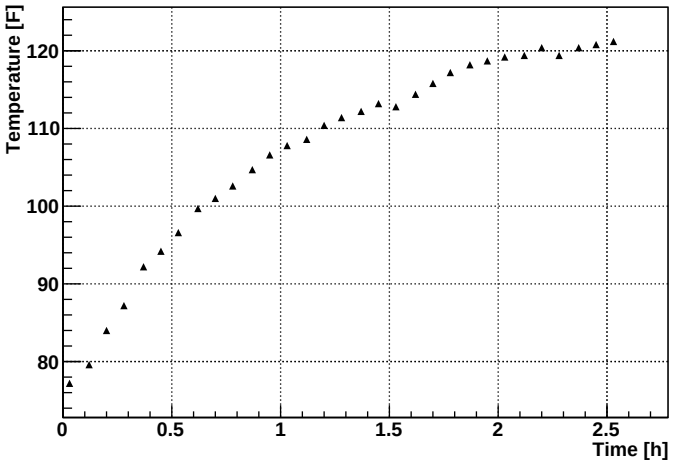

Figure 3.10: Expected Magnet's temperature as a function of time for a current of 100 Amp. Data from D. Jensen

Table 3.1: Beam sheet of the Tertiary Beamline. Positions measured from target

	Height	Width	Z	X
ToF scintillator 1	55 mm	152 mm	55.1 in	15.9 in
Wirechamber 1	64 mm	178 mm	70.0 in	20.1 in
Wirechamber 2	106 mm	305 mm	137.2 in	39.3 in
Wirechamber 3	150 mm	305 mm	212.3 in	52.3 in
Wirechamber 4	192 mm	406 mm	282.3 in	61.6 in
ToF scintillator 2	200 mm	508 mm	296.9 in	61.6 in

where cosmic rays are taken for testing each electronic stage. Figure 3.7 shows the position of the four tracking stations along the beamline. The Tertiary beam was specifically design to maximize the yield, so the active area of each tracking station varies. The dimensions of the wire chambers to maximize the acceptance of the Tertiary Beam as well as its ZX position along the beamline is summarized on table 3.1.

The total material in each chamber should add an effective length distortion of 0.2% χ_0 and 0.07% λ_I. So the main resolution is driven by the inter - station space and the multiple scattering, that is, with 70 inches of air between chambers, the spectrometer allows a momentum resolution below 1% in the energy range required. It is also possible to reach half that resolution if air is replaced by helium bags. Figure 3.13 shows the computed effect of multiple scattering and tracking error for the current baseline. This figure evinces the dominant effect

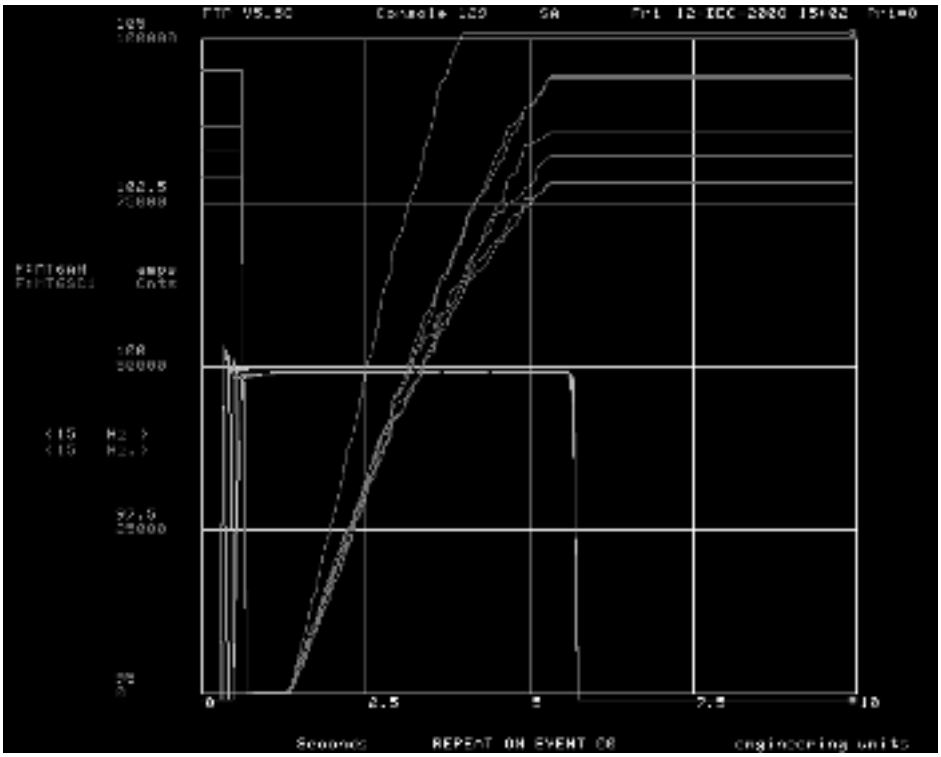

Figure 3.11: Magnet's current measured from ACNET for seven spills showing the synchronization with spill gate. The square pulse is the current supplied to the magnet and the ramping signal comes from the scintillator counter just upstream the target. (D. Jensen)

of multiple scattering at low energies, while at high energies the main source of error is due to the short baseline, driven exclusively by the resolution of the wire chambers. The baseline was calibrated in order to minimize the sigma for the momentum reconstruction.

The time of flight (ToF) system

Once the momentum and trajectory have been reconstructed, a time of flight system will be used as a particle identifier. This system has two scintillator counters placed at both ends of the baseline. The dimensions and positions of these scintillator counters are given in table 3.1. Currently the ToF system is under construction by MINERνA. A rectangular plastic scintillator with two photomultipliers per station is sufficient for the desired resolution. Studies of reconstruction, in section 3.2.3, point out that a resolution of about 100 - 150 ps in each counter is enough to provide a proper particle identification.

The ToF system has the following two tasks: to provide a fixed-flow trigger

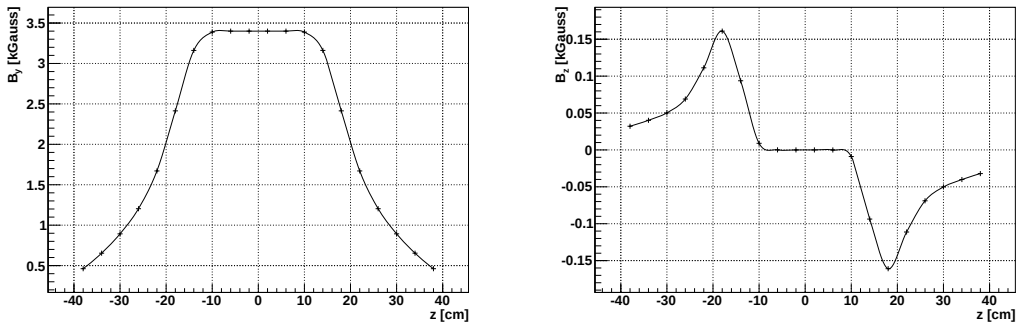

(a) B_y along the axis (b) B_z along the axis

Figure 3.12: Simulated fringe fields

to the DAQ and to measure the actual time interval that the triggering particle takes to travels from one counter to the other.

Figure 3.14 shows the expected ToF signature produced for a beam consisting on 15 M 16 GeV pions on target. From this picture, we see that the first five nanoseconds of signal are filled with pions. After that protons develop in a flat distribution. The first two nanoseconds, on the other hand, are populated by fast e^+ - e^-.

As it was discussed at the beginning of this chapter, the meson beam results form a macroscopic extraction of the MI. The actual time distribution of the beam is flat over the whole 3 seconds. That is, for a spill 300k pions on our target, we will have one particle every 10 μs. Even though this was not included in the Monte Carlo, studies on multiplicity at the scintillator counters show that the DAQ system for a ToF trigger scheme working at 15kHz could safely handle the event rate at the Tertiary Beam, see figure 3.15. Based on the production rate, the probability of double occupancy is also reduced to up to about 5%.

On the next section, I use all this information to propose a trigger system to separate the hadron from the lepton signal.

Expected signal at the testbeam detector

The integrated magnetic field for the couple of dipoles defines the ΔP in the plane ZX. Introducing the appropriate element's values one gets

$$\Delta P = e \int \vec{B} \cdot d\vec{l} \sim 100\, MeV/c.$$

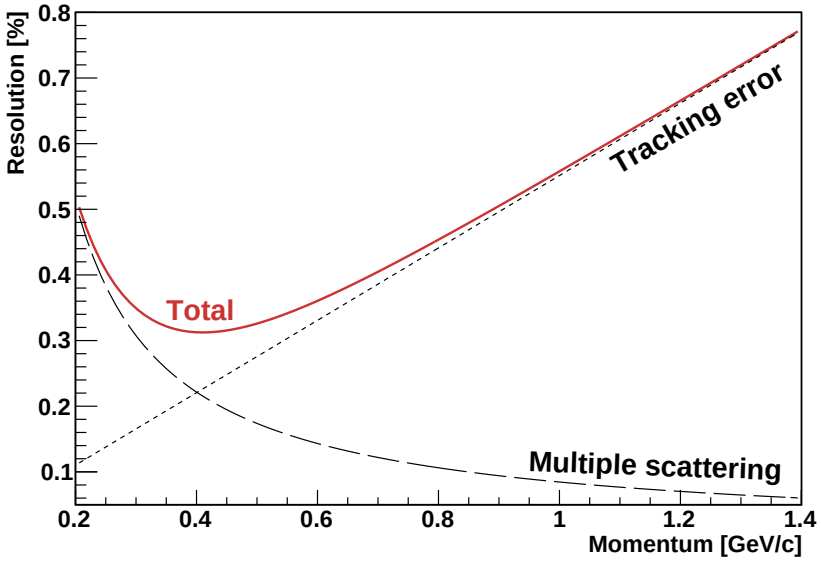

Figure 3.13: Computed momentum resolution for pions through the beamline. The tracking error is calculated based on the distance between the wire chambers and their pitch. The multiple scattering error is calculated considering air.

So we expect a high suppression of particles with momentum below 100 MeV only due to the geometry.

I used g4beamline to model the whole beamline as described by figure 3.7. The geant4 physics list QGSPBIC was used for the production and transport of particles through the target and collimator. The g4beamline source script used in the simulation of the complete chain is provided in the appendix.

The particles that having satisfied the trigger criteria hit the TestBeam detector are shown in figure 3.16 and 3.17. Notice the beam in the energy range require is mainly composed by pions and protons, peaking at 600 MeV/c. Notice also that the low momentum component has been decreased by a large factor compared to the beam coming out from the collimator (figure 3.5) as expected.

Figure 3.18 shows the correlation due to beamline size between momentum and time of flight of truths at the TestBeam detector. Notice how the non-relativistic protons arrive almost four nanoseconds after the fastest electrons. This could provide a trigger method based on delays for filtering events with protons hitting the MINERνA detector. This property can be easily double check in future measurements.

The spectrometer also introduce a correlation between momentum and the x-position. Figure 3.19 shows a scatter plot of this correlation. However, this is

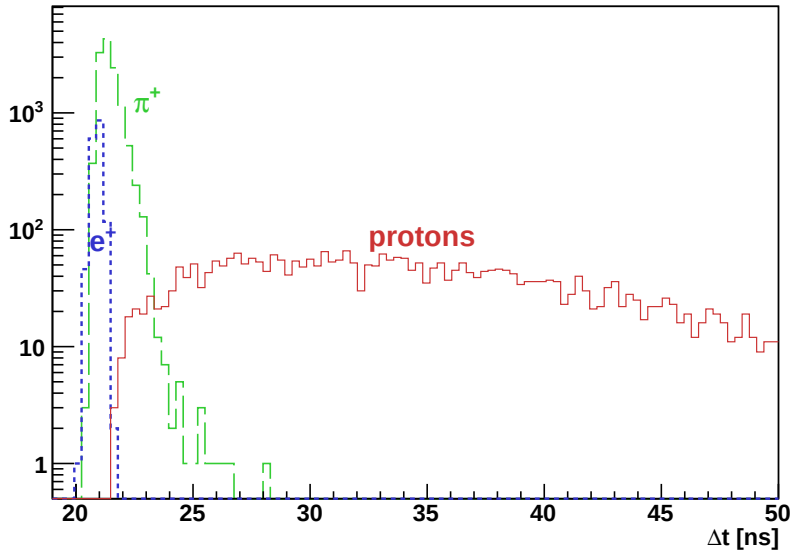

Figure 3.14: Time of flight of truths hitting the MINERνA detector. Note the late development of the hadronic tail.

diffused mainly because the beam spot is wide and has an angular distribution around 16°.

3.2.3 The reconstruction

The trigger

As it was discussed above one can use the Time of Flight coincidence to construct a fixed-flow trigger for selecting hadrons from the tertiary beam. To achieve that an optimal choice of discriminator gates and coincidence arithmetics has to be made. Figure 3.14 shows the expected time of flight for the beam using a smearing of $\sigma = 150$ ps in each counter. Based on this a delay in ToF2 can be tuned so that we only trigger on slow particles, see scheme at figure 3.20.

Reconstruction's algorithm template

The main reconstruction scheme is as follows:

- Position information is extracted from the wire chambers with $\sigma = 0.5$ mm.
- Timing information is extracted from the scintillator counters with $\sigma = 150$ ps.

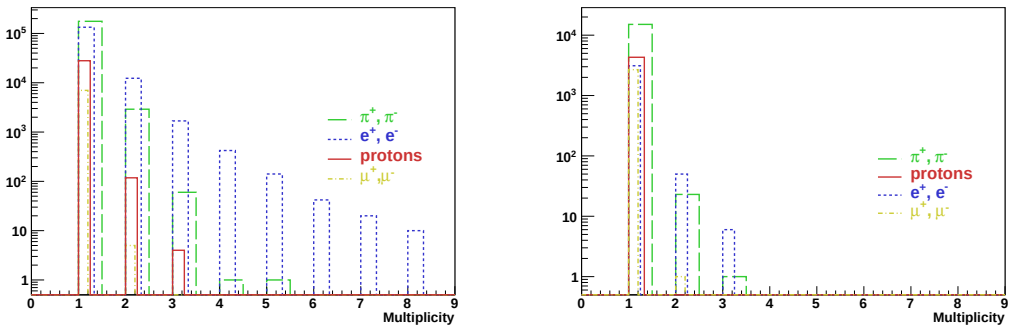

(a) ToF1 Counter (b) ToF2 Counter

Figure 3.15: Multiplicity in time of flight counters for 50 spills. Less than 10% of the time there might be a double ocuppancy per trigger.

The momentum as a function of the bending angle is given by [22] $p_{xz} = \frac{e}{\sin\theta}\int Bdl$, where $\theta = \theta_2 - \theta_1$ is provided by the measurements with the wire chambers. Once the momentum is computed, the time of flight measurement will provide the mass of the particle, thus the identification is complete.

In the appendix, I provide a basic source script for reconstruction of the tertiaries that trigger. The algorithm was implemented also in MINERνA's GAUDI Framework for future improvements. This algorithm takes MC simulation data and mimics the behavior of the beamline elements. It provides a reconstructed signal from the DAQ and a contrast with MC truths.

Figures on 3.21 show the comparison of the output of my primitive reconstruction template and the MC truth for a nominal spill of the tertiary beam. Notice that with this naive template we can isolate the proton signal very well, but the segregation of pions and positrons may need a better reproduction of the magnetic field, which for the present algorithm it is only a constant integrated field.

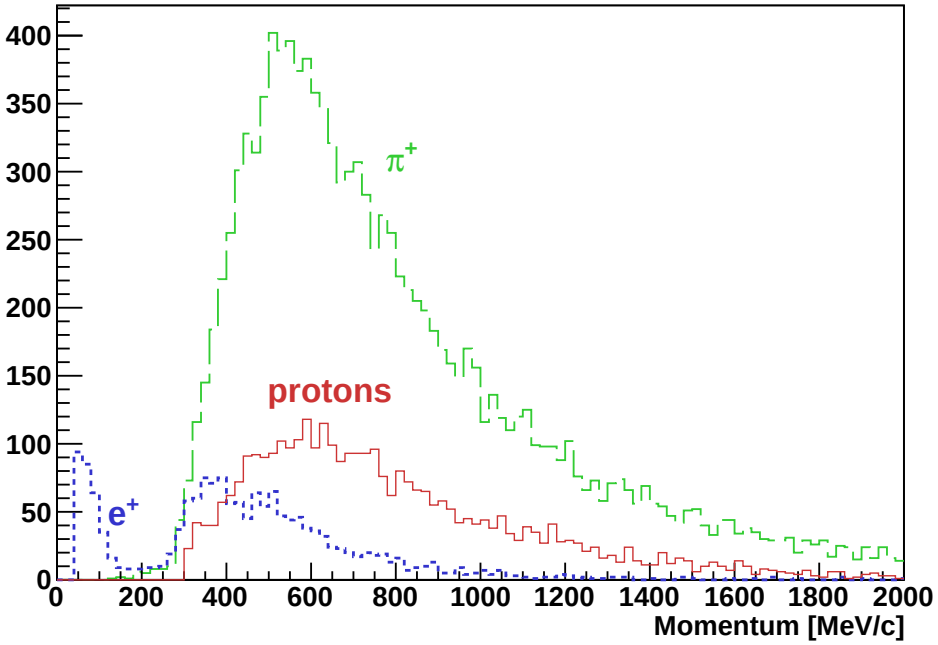

Figure 3.16: Momenta spectrum of truths hitting the MINERνA detector. Signal generated by 15M pions on target.

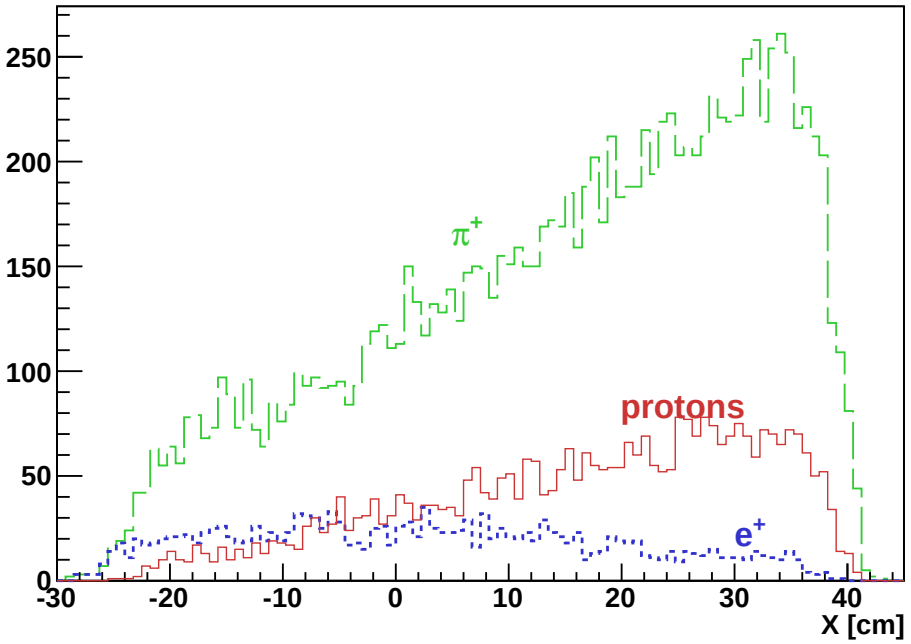

Figure 3.17: Horizontal incidence of truths hitting the MINERνA detector integrated over y for 15M pions on target.

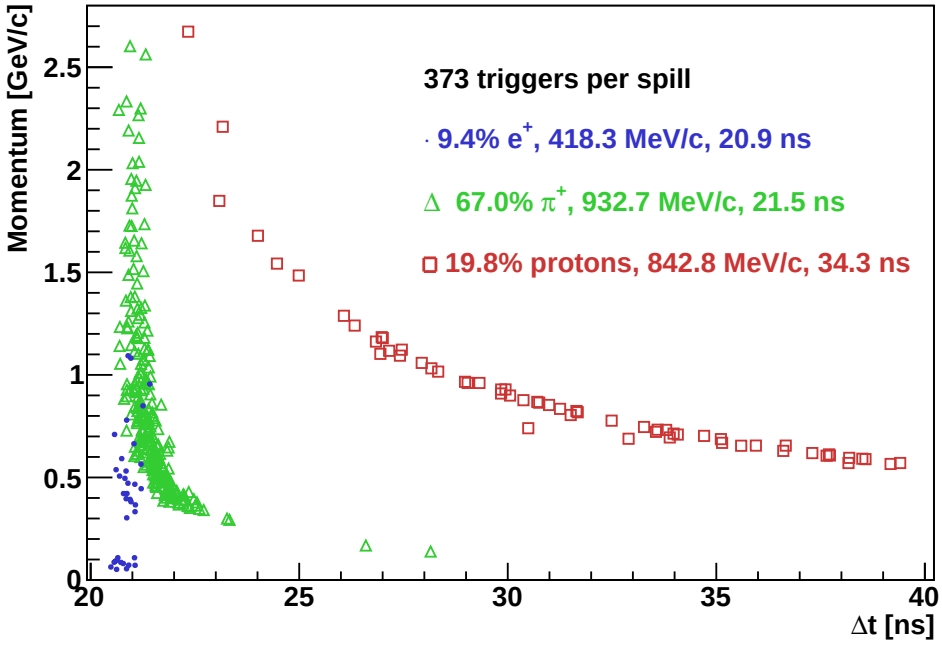

Figure 3.18: Momentum and time correlation of truths hitting the MINERνA detector. Signal generated by 300K pions on target. The mean values can be extracted from the legend.

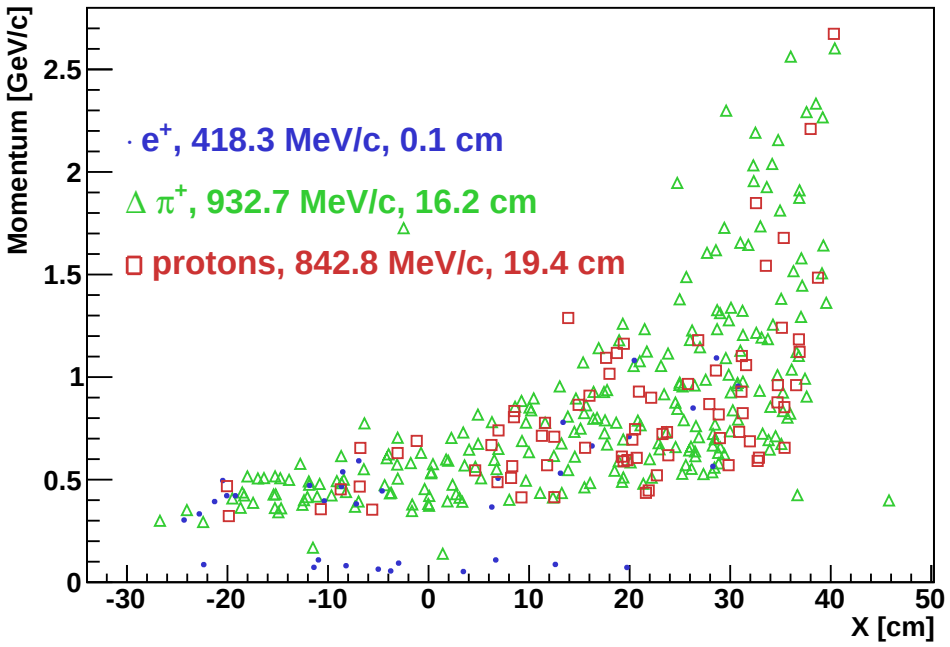

Figure 3.19: Momentum and position correlation of truths hitting the MINERνA detector. Signal generated by 300K pions on target. The mean values can be extracted from the legend.

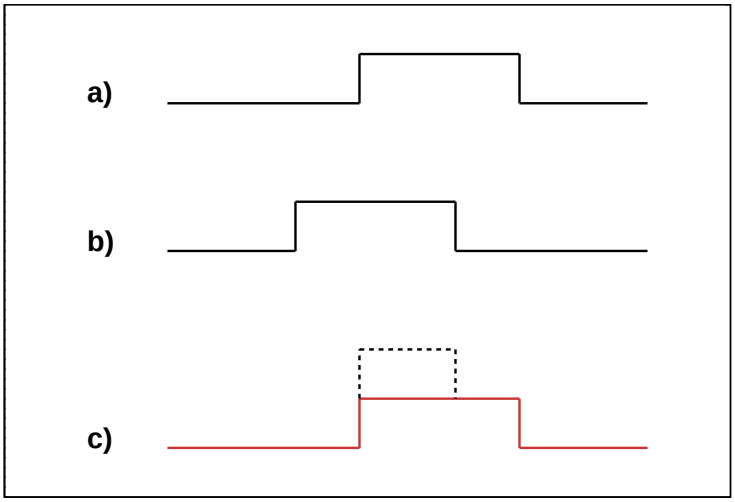

Figure 3.20: Common coincidence trigger. a) Signal coming from first counter. b) Signal coming from second counter with appropriate delay ($\sim$ 22 ns + NIM width from discriminator). c) a$\times$b and coincidence signal in common start

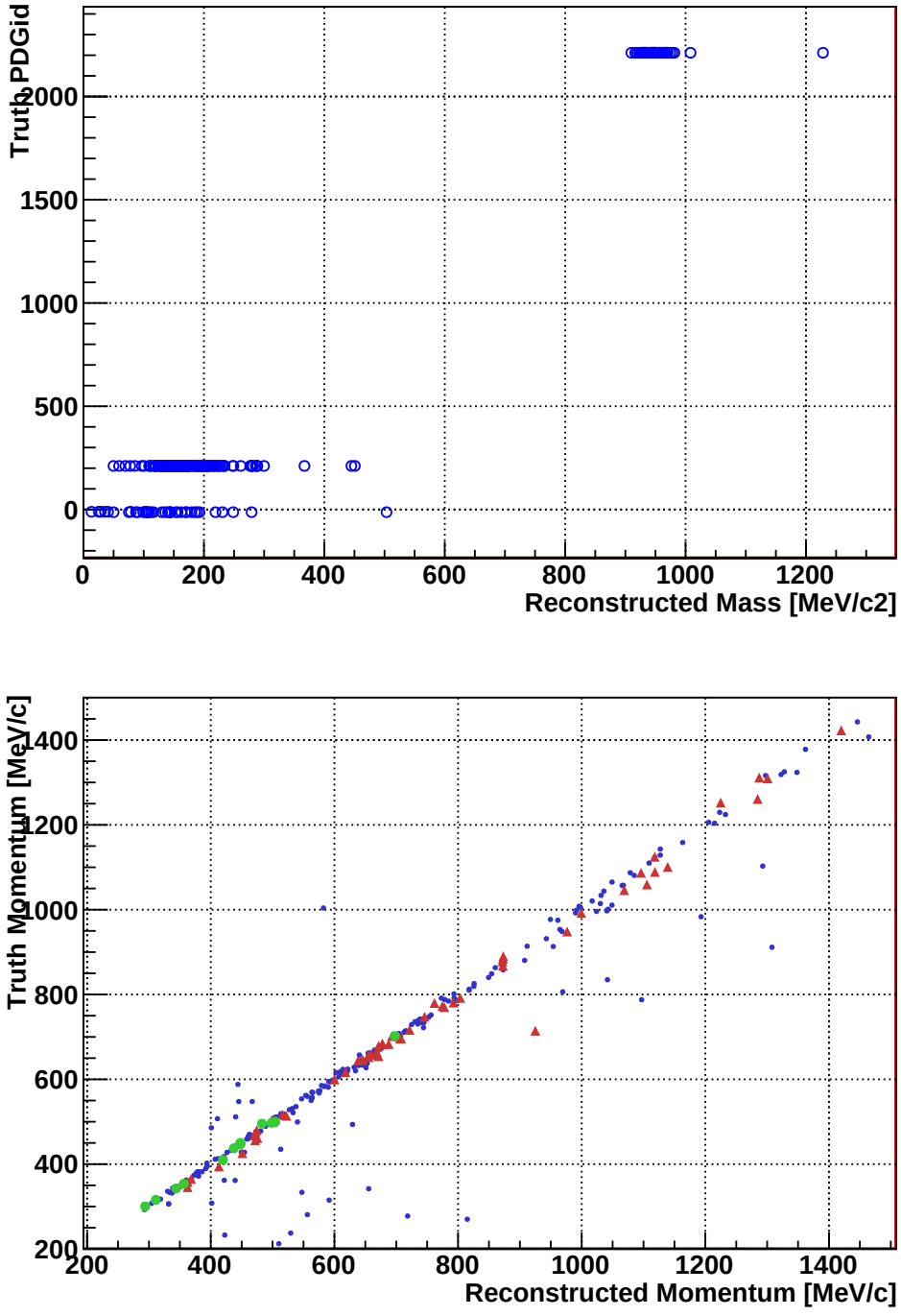

Figure 3.21: Particle identification and momentum reconstruction using the reconstruction algorithm on MC data with proper smearing.

Chapter 4

Commissioning and first test of the beam

In October 2008, there was a test of the tertiary beam at MTest. By that time only the target and collimator were ready. We use all the space available at MTest to check the species of the *Tertiary Beam*. In order to achieve this goal a couple of scintillator counters separated by about 8.5 meters and a lead glass block at the end of the beamline gave us the timing and the electron hadron separation for this specific test. A complete report on the results of the test run was published by the MINERνA TestBeam team [23]. Here I will point out the some of the most important results.

4.1 Beamline elements

Target and collimator

The copper target and the steel collimator, discussed in the previous chapter, were machined by Fermilab's Mechanical Division on August 2008. As the beam comes at 65 inches above floor level, they also made suitable stands for these elements. A natural extension of the collimator was include to support the target. The collimator's stand, due to a clever rail system, allows the tertiary beam to be removable from the main beamline. This is extremely useful when switching between high and low energy beams.

Figure 4.1 shows the copper target and its support. A coin was included on the photograph for scaling. After three weeks of exposure to a 16 GeV beam, the target was proved to be relatively stable, for measurements on its activity

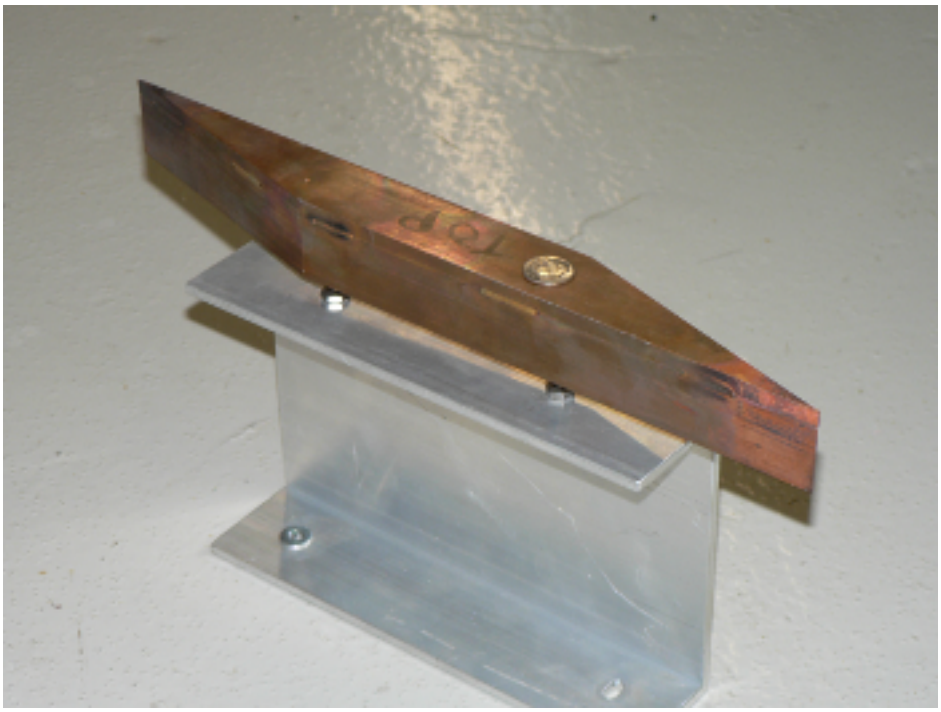

Figure 4.1: Copper target and aluminum stand for installation. A dime was included for scaling

reported much less than 1mR/h and was classified as a Class I target in Fermilab's radiation scale, see [24].

On the other hand, the collimator was not made by a single piece as the target. Due to its geometrical requirements, it was welded by layers with special care in the channel region. Picture 4.2 shows half the collimator while it was in production. The bottom layer extends so that the target can be bolt in it. The third layer, the thinnest, was fragmented so that it shapes out the channel, the remaining layers complete in a symmetrical way the height of the collimator and center the channel vertically. Measurements regarding radiation hazards were made during the test run and showed that the collimator damped the punch-through pretty well.

Time of Flight System

The tracking chambers, scintillator counters and magnets were not ready for this test run. However we could use the ToF scintillator from MTest to measure the time of flight of particles coming from the channel. The preparation, calibration and operation of this ToF system was done by R. Gran, C. Araujo and Z. Gutierrez and is extensively discussed on [25].

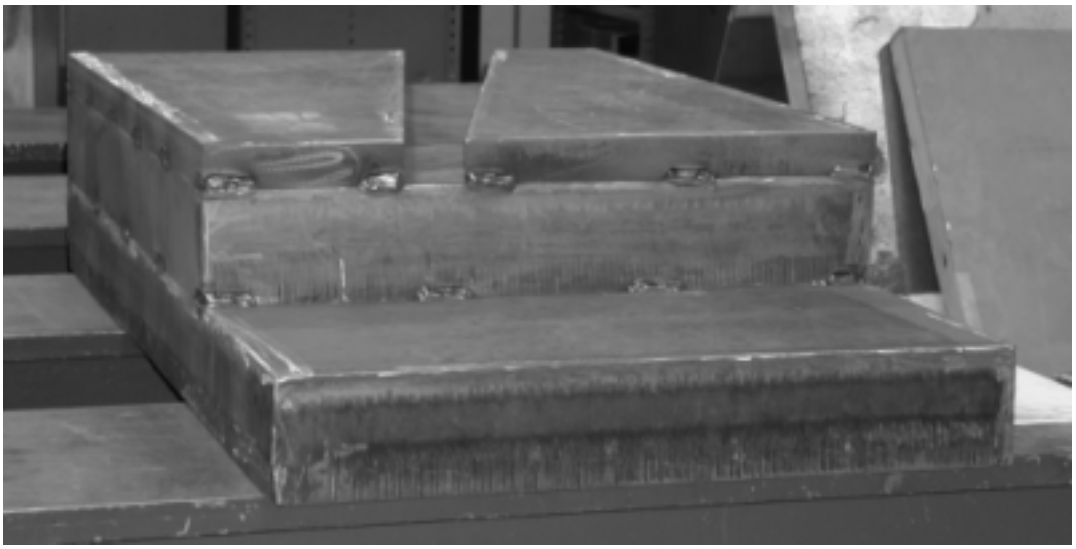

Figure 4.2: Sandwich steel collimator. The top has been remove to show channel details.

The size of this counters allowed only a measurement of a small part of the beam. Each counter is an regular octagon parallelepiped, see figure 4.3, with an area of 482.8 cm^2 and 2 cm of thickness that covered only a third of the beam width at the farthest station. Four photomultiplier tubes are symmetrically attached to the scintillator.

Studies performed with these scintillators in a 120 GeV/c proton beam [25] show that this system could reach up to 150 ps resolution. The pmt signal was connected to constant fraction discriminators and a simple coincidence system. For our test run the coincidence was set to common start and the width of the gate and delays were suitable for a complete capture of the signal. No implementation of the special triggering system described in the previous chapter was made during this test run.

4.2 Data acquisition system

We used the NIM electronics available at MTest. The specific modules we used are

- ORTEC 934 Constant Fraction Discriminator,
- LeCroy 365 Logic Unit,
- LeCroy 622 Quad Coincidence,

Figure 4.3: Time of flight scintillator unit used in this commissioning.

- Phillips 7186 16-Channel TDC,
- LeCroy 2249A 12-Channel Charge ADC.

The scintillator's pmts were coupled to the TDC, through a discriminator, and provided the main data from this test run. The lead glass' pmt was coupled to an ADC channel previously calibrated with 2 GeV electrons. The system was triggered by the coincident signal of both scintillators. Figure 4.5 shows a drawing of the beamline elements used in this test run.

4.3 MonteCarlo Predictions

The beam coming from the channel should be the mixed beam we predicted in the previous chapter. Even though the diversity of momenta could not be measured directly, we expect a particular timing spectrum due the difference in particles' velocities, specially of those hadrons which are non-relativistic. Thus, the different particle production rate could be discernible from the time of flight spectra; the Montecarlo simulation supports this fact.

Figure 4.4: MTest data acquisition electronics.

The hadron production was also checked due to a couple more devices installed on the beamline. The first was a lead sheet of 1.5 cm of thickness just after the collimator's channel so that many electrons were killed by showering and/or multiple scattering. The second tool was a Cerenkov detector (lead glass) at the end of the beamline, just after the second scintillator. Measurements of the light collected by a pmt coupled to the lead glass showed the difference between signal from fast electrons and signal from minimum ionizing particles.

In order to understand the measurements, I made a variation to the Monte-carlo model to include this particular geometry. An extension of the baseline was implemented so that all the space in the hall was used. Besides the fact that the simulation ran in a 64 double-core-node cluster, I had to make a kinetic energy cut to reduce the computing time. A cut in kinetic energy of 50 MeV, which will leave the effective electron component intact but may have a high impact on the slow proton and pion component, was used. That leaves a sub estimation of the rate for protons below 300 MeV/c and for pions below 150 MeV/c.

The simulation reports a pions spectrum with a broad momentum distribution from a few hundred MeV/c to a few thousand MeV/c, which is the main population of the spill. The protons spectrum is also broad. It is important to notice that the early signal corresponds to very low momentum positrons, see

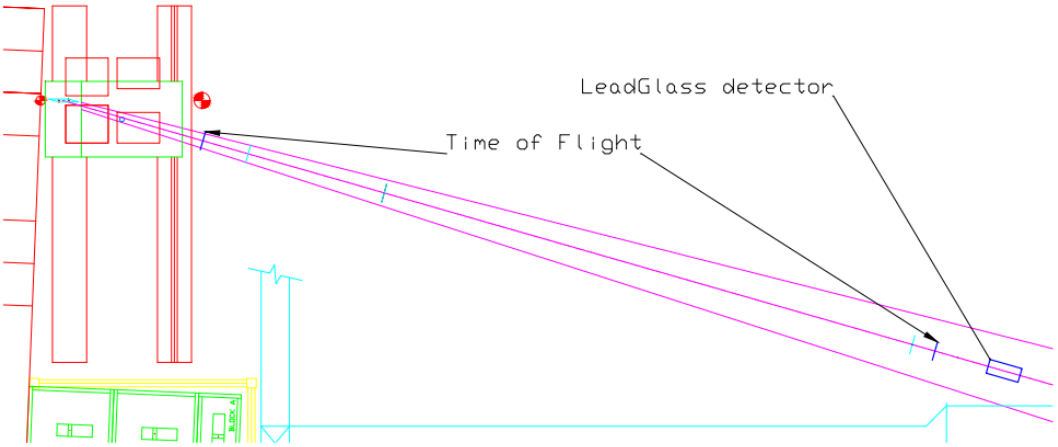

Figure 4.5: Beamline for the test run

figures 4.6 and 4.7.

Furthermore the Montecarlo also shows that we should expect a ToF signal with a narrow peak due to the electronic component focused on the first nanosecond (smearing of $\sigma \sim 150$ ps). The fastest pions overlap this first nanosecond and extends for about 2 nanoseconds for slow pions. After that only the slow proton component remains. This signature is shown in figure 4.6 where we have smeared the time with a gaussian resolution that accounts for that of the scintillators.

4.4 Running modes and data analysis

We were authorized to have beam 12 hours a day for almost three weeks. After one day of calibration in the secondary beam, we placed the target and collimator and used the beamline to analyze the production of tertiaries. We took data with an incoming beam of 8 GeV and 16 GeV energy with the standard configuration. We also took runs adding a lead converter, changing the position of the detectors and changing the beam centrality. All these modes can be summarized as follows:

- 8 GeV/c
- 8 GeV/c with lead converter
- 16 GeV/c
- 16 GeV/c with lead converter
- 16 GeV/c with reversed polarity

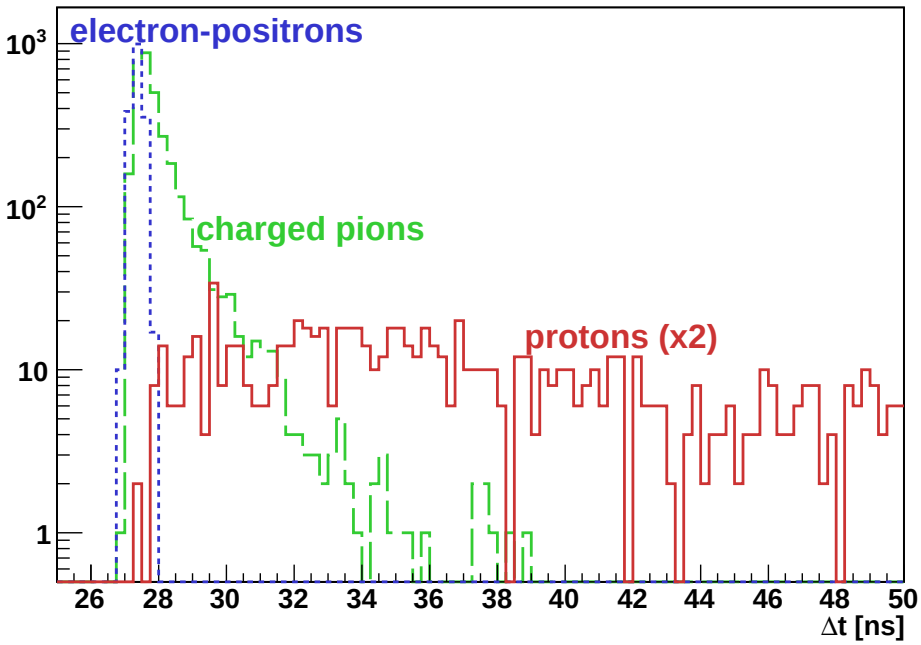

Figure 4.6: Time of flight of truths hitting the second scintilator and coming from a coincidence on trigger. For 15M pions on target.

- 16 GeV/c with secondary beam off center
- 16 GeV/c with second scintillator counter off center

The peculiarities of these runs can be found in the MINERνA's logbook [26]. Different modes of beam extraction, often called SY120 operations, were used. Due to various factors, to fairly compare these results one has to applied a proper normalization to the data. Details on how we did these and much more technical information of this test was reported extensively on [23].

The are many detectors upstream the *tertiary beam* wich can monitor the position and quality of the incoming beam. The information of this detectors can be obtained via the ACNET platform. The most important ones are the SWC1H/SWC1V (wire chambers for horizontal and vertical beam profile) and MTSC6 (fast scintillator counter for beam intensity).

There were many things that we learned about the beamline with this test run. However due to a deficient record of all the variables that affected the production, ie. extraction mode of the main beam, slow DAQ rates and non-flushed buffers, missing data time stamping, etc., this first test can only provide a qualitative expectancy of the beam content. Further tests, to be hold on early 2010, will

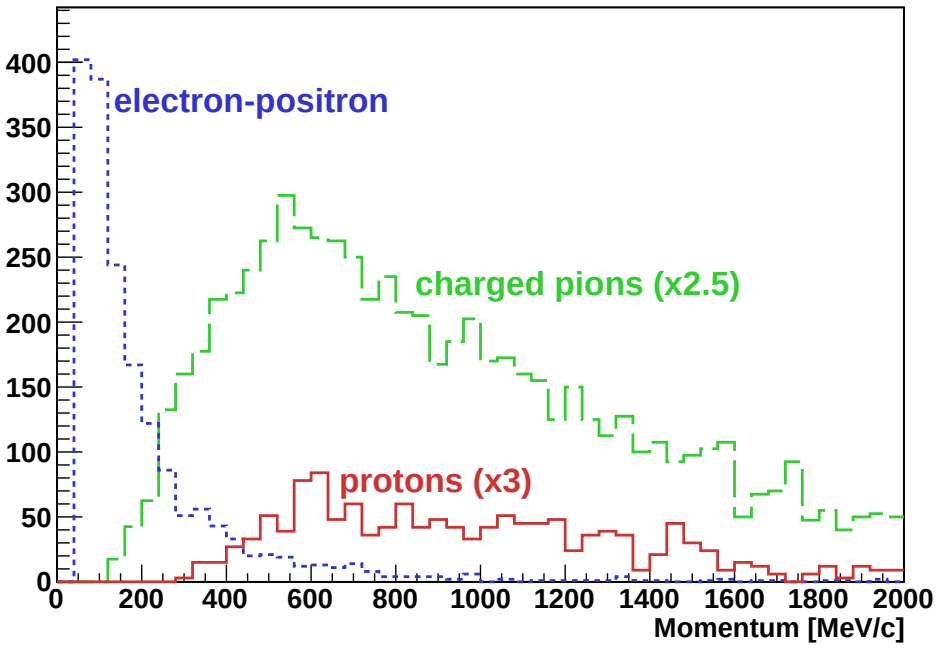

Figure 4.7: Momentum distribution of truths hitting the second scintilator and coming from a coincidence on trigger. For 15M pions on target.

measure the characteristics of the tertiary beam with a more systematic control of the tuning parameters of the beam and efficiency of detectors and readout.

By the end of December 2008, Richard Gran and I wrote a document [23] for the MINERνA document server with all the details of October's test run. Here I will point out only the most important information extracted form the data.

A rough estimation of the efficiency of the detectors were made based on the average number of particles on target, efficiency in the readout system (which varies according to the time structure of the beam) and efficiency in the digitalized signal from the pmts. This calibration constant was [27]

$$(1.16 \times \text{POT counted by MT6SC1}) \times \frac{\text{Events recorded}}{\text{Coincidences}} \times \frac{\text{Well digitalized events}}{\text{Events recorded}},$$

where the 1.16 factor arise from the fact that we used a scintillator upstream the target (MT6SC1) to measure the number of particles on target. This scintillator, however, has an efficiency of 95% and a blindness to double particle occupancy in the same bucket, which we expect to have 10% of the time. The second and third factors introduce the efficiency of the detectors and the DAQ.

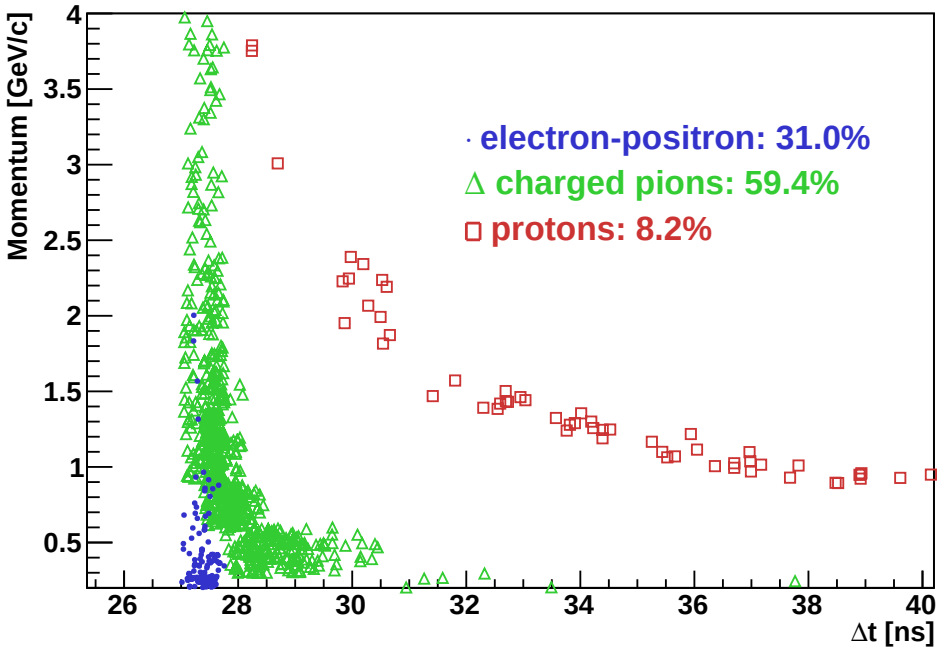

Figure 4.8: Momentum and time correlation of truths hitting the second scintilator and coming from a coincidence on trigger. For 3M pions on target.

Once normalized, the measurements report a high reduction of particles for the lead run at the first two nanoseconds of signal. Figure 4.9 shows this effect quantitatively as we made a per-bin division of the two data samples. Notice how the fastest signal (mostly e^+ e^- content) is highly suppressed. The Montecarlo, figure 4.10, shows the same effect and the same ratio. We expect that the sub estimation of the slow proton component, due to the cuts mention above, affect the ratio on the tail as well.

Figure 4.11 shows the light collected at the lead glass as a function of the particle time of flight. A direct comparison with figure 4.8 can not be done due to the lead glass behavior with heavy charged particles [1]. However we can see a clear signature of the electronic component mainly localized between 27 ns and 28 ns and ramping all the way to high charge. The signature of minimum ionizing pions, located at about 60 pC, is also evident. The lead glass block has about 50 cm of length, so the slow heavy component will be trapped within it lowering the charge at the lead glass at the end of its range [1], this effect may explain the drop in charge for the slow component which is evident in figure 4.12. The same inspect at the lead glass shows a high reduction on the e^+ e^- component.

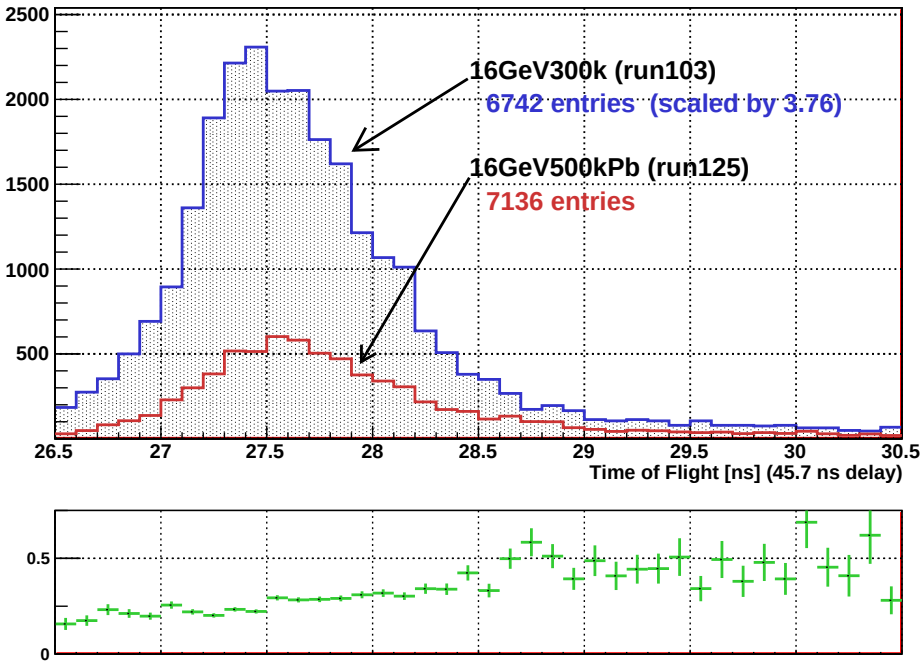

Figure 4.9: Raw data from the time of flight measurement. Run103 corresponds to a direct measurement of the particle coming out from the collimator. Run125 corresponds to a run with a lead converter placed downstream the collimator.

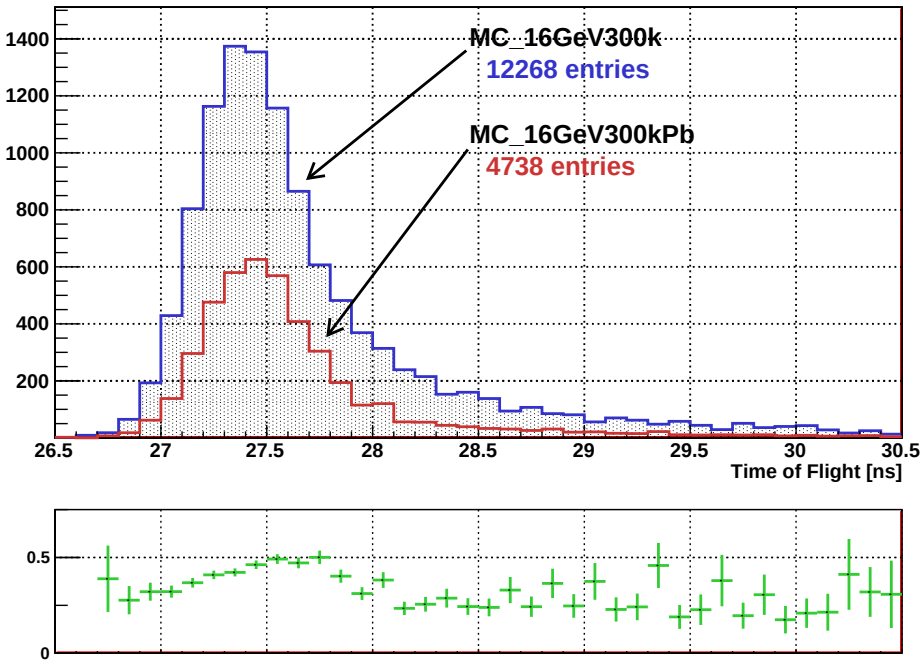

Figure 4.10: MonteCarlo simulation of the expected time of flight for particles coming out from the collimator with the test run geometry.

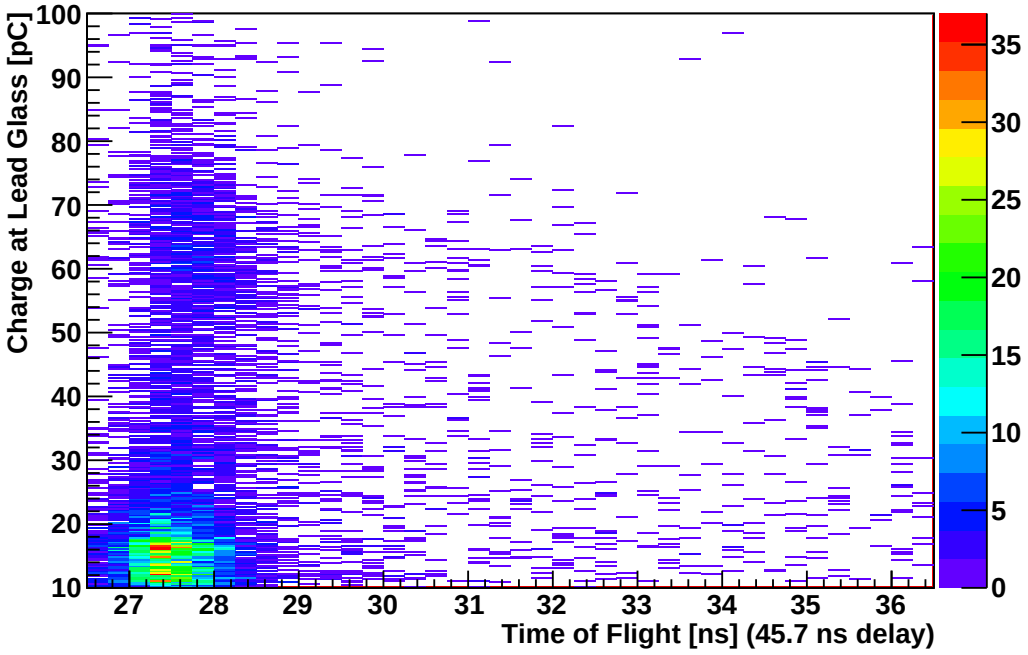

Figure 4.11: Measured time of flight vs light collected from lead glass for a run with 16 GeV particle on target.

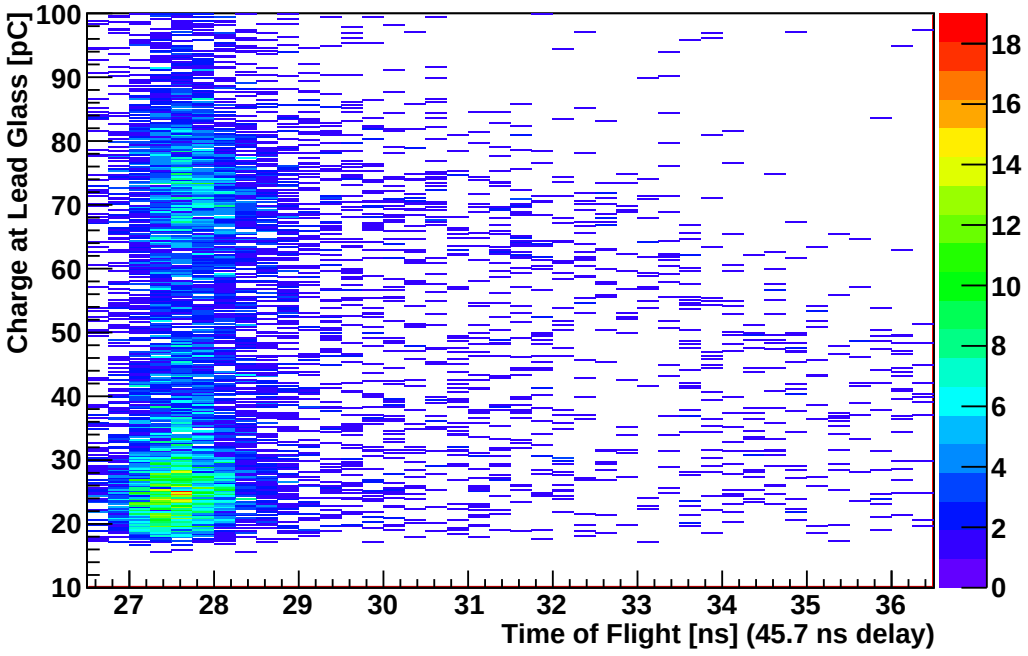

Figure 4.12: Measured time of flight vs light collected from lead glass for a run with 16 GeV particle on target when the lead converter was placed.

Chapter 5

Conclusions and Outlook

This document presents the main considerations taken for the design of the low energy hadron beam as well as the measurements obtained by the first test which make it looks very promising. The construction of the beamline will be finished by summer 2010 where a complete and systematic test will be performed.

Chapter 3 explained the reasons that guided us to choose the particular dimensions and shape of the target to produce the tertiaries. In addition there was listed all the beamline elements and their functions in order to provide a proper particle identification and momentum selection. It was shown also that with this beamline we would be able to differentiate protons from pions through the time of flight as well as estimate any particle's momentum below 1 GeV with a reasonable accuracy.

The first test of the beam reports clearly that the target and collimator design were producing particles in the range expected. These results are summarized in chapter 4 where the TDC signal of a primitive time of flight system was our main probe. According to these measurements the time spectrum of the beam resembles that of the simulation. Furthermore measurements with a led converter and a lead glass points out that the population of the electron positron component is localized at the first couple of nanoseconds.

A spectrometer developing up to 0.3 Tm integrated field should be enough to select mostly particles at 600 MeV/c. Considering the current tracking resolution this spectrometer should be able to provide a good accuracy in the reconstruction of momenta up to 1.5 GeV. Future measurements will help to completely characterize the tertiary beam and will provide new possible uses.

The tertiary beam by itself offers a powerful tool due to it particularly low

energy and hadron discrimination for experiments beyond MINERνA.

Appendix A

Source scripts

A.1 G4Beamline source script

```
param worldMaterial='Air'
physics QGSP_BIC
param histoFile="QGSPBIC-2us"
#trackcuts maxTime=2000
trackcuts kineticEnergyCut=50

param in=25.4
param cm=10
param killing=0

#world
box wall length=2 kill=1
 place wall rename=south width=96*$in height=50*$in  z=-6*$in-1 x=+36*$in
 place wall rename=north width=96*$in height=50*$in  z=365*$in+1 x=+36*$in
 place wall rename=west  width=371*$in height=50*$in  z=179.5*$in x=+36*$in-48*$in-1 rotation="Y90"
 place wall rename=east  width=371*$in height=50*$in  z=179.5*$in x=+36*$in+48*$in+1 rotation="Y90"
 place wall rename=up    width=96*$in height=371*$in z=179.5*$in x=+36*$in y=-25*$in-1 rotation="X90"
 place wall rename=down  width=96*$in height=371*$in z=179.5*$in x=+36*$in y=+25*$in+1 rotation="X90"

#beam
param -unset BeaEve=200 # events
param -unset BeaFir=1  # first event
param BeaLas=$BeaFir+$BeaEve-1
param histoFile="16GeV-T1-$histoFile-$BeaFir-$BeaLas"
beam gaussian particle=pi+ meanMomentum=16000 meanT=-0.06 nEvents=$BeaEve*0.005 firstEvent=$BeaFir \
          beamZ=-5.97*$in sigmaX=11 sigmaY=7
param BeaFir=$BeaFir+$BeaEve*0.005
beam gaussian particle=pi+ meanMomentum=16000 meanT=-0.04 nEvents=$BeaEve*0.005 firstEvent=$BeaFir \
          beamZ=-5.97*$in sigmaX=11 sigmaY=7
param BeaFir=$BeaFir+$BeaEve*0.005
beam gaussian particle=pi+ meanMomentum=16000 meanT=-0.02 nEvents=$BeaEve*0.005 firstEvent=$BeaFir \
          beamZ=-5.97*$in sigmaX=11 sigmaY=7
param BeaFir=$BeaFir+$BeaEve*0.005
beam gaussian particle=pi+ meanMomentum=16000 meanT=0.00 nEvents=$BeaEve*0.90 firstEvent=$BeaFir \
          beamZ=-5.97*$in sigmaX=11 sigmaY=7
param BeaFir=$BeaFir+$BeaEve*0.90
beam gaussian particle=e-  meanMomentum=16000 meanT=0.00 nEvents=$BeaEve*0.07 firstEvent=$BeaFir \
          beamZ=-5.97*$in sigmaX=11 sigmaY=7
param BeaFir=$BeaFir+$BeaEve*0.07
beam gaussian particle=pi+ meanMomentum=16000 meanT=+0.02 nEvents=$BeaEve*0.005 firstEvent=$BeaFir \
          beamZ=-5.97*$in sigmaX=11 sigmaY=7
param BeaFir=$BeaFir+$BeaEve*0.005
beam gaussian particle=pi+ meanMomentum=16000 meanT=+0.04 nEvents=$BeaEve*0.005 firstEvent=$BeaFir \
          beamZ=-5.97*$in sigmaX=11 sigmaY=7
param BeaFir=$BeaFir+$BeaEve*0.005
beam gaussian particle=pi+ meanMomentum=16000 meanT=+0.06 nEvents=$BeaEve*0.005 firstEvent=$BeaFir \
```

```
        beamZ=-5.97*$in sigmaX=11 sigmaY=7

virtualdetector fd color=0,1,0 require="Pz>0"
place fd rename=BEAM width=110 height=70 z=-5.94*$in

#target
if (1)
  place wall rename=twest  width=13*$in height=4*$in  z=0.5*$in x=-8*$in-1 rotation="Y90"
  place wall rename=teast  width=13*$in height=4*$in  z=0.5*$in x=+8*$in+1 rotation="Y90"
  place wall rename=tup    width=16*$in height=13*$in z=0.5*$in y=-2*$in-1 rotation="X90"
  place wall rename=tdown  width=16*$in height=13*$in z=0.5*$in y=+2*$in+1 rotation="X90"
  trap Target height=2.280*$in length=1.250*$in color=1,0.6,0 material="Cu" \
            Xul=-6.243*$in Xur=-1.708*$in Xll=+1.708*$in Xlr=+6.243*$in
  place Target z=+0.516*$in rotation="Z-74,X-90"
endif

param MagAng=16/180*3.141592654
#collimator
if (1)
  param Co1ZPo=7.971*$in  # z position of first face of collimator
  param Co1XPo=7.971*$in  # x position of first face of collimator
  param Co1Len=42.756*$in # length
  param Co1Wid=32.000*$in # width
  param Co1Hei=57.0*$cm   # height
  param Co1Mat="Fe"       # material
  param chnHt=5.3*$cm     # height of channel
  box Co1Pw3 length=$Co1Len material=$Co1Mat color=0.55,0.6,0.5 height=($Co1Hei-$chnHt)/2 width=$Co1Wid \
            kill=$killing
  extrusion Co1Pw1 length=$chnHt color=0.55,0.6,0.5 material=$Co1Mat kill=$killing \
  vertices="202.46,-205.486;202.46,21.336;1288.466,296.0624;1288.466,-205.486"
  extrusion Co1Pw2 length=$chnHt color=0.55,0.6,0.5 material=$Co1Mat kill=$killing \
  vertices="202.46,95.4532;202.46,607.314;1288.466,607.314;1288.466,444.2206"
  place Co1Pw1 z=0 rotation="X-90,Y-90"
  place Co1Pw2 z=0 rotation="X-90,Y-90"
  place Co1Pw3 rename=Co1Pw3 z=$Co1ZPo+$Co1Len/2 y=+($Co1Hei+$chnHt)/4 x=$Co1XPo
  place Co1Pw3 rename=Co1Pw4 z=$Co1ZPo+$Co1Len/2 y=-($Co1Hei+$chnHt)/4 x=$Co1XPo
endif

#tof scintillators
box sci material='POLYSTYRENE' color=0.7,0.7,0.4 length=2*$cm
place fd  rename=ToF1 rotation=Y16 width=6*$in height=5.5*$cm \
          z=55.533*$in-1.1*$cm*cos($MagAng) x=15.924*$in-1.1*$cm*sin($MagAng)
place sci rename=sci1 rotation=Y16 width=6*$in height=5.5*$cm \
          z=55.533*$in                       x=15.924*$in
place fd  rename=ToF2 width=20*$in height=20*$cm \
          z=297.336*$in-1.1*$cm              x=49.788*$in+30*$cm
place sci rename=sci1 width=20*$in height=20*$cm \
          z=297.336*$in                       x=49.788*$in+30*$cm

#magnets
if (1)
  param MagFie=0.34
  genericbend Trim By=$MagFie fringeFactor=1 fieldWidth=30*$cm  fieldHeight=15*$cm \
            ironWidth=50*$cm ironHeight=35*$cm fieldLength=50*$cm ironLength=50*$cm kill=$killing
  place Trim rename=Trim1 rotation=Y16 z=156.062*$in x=44.750*$in
  place Trim rename=Trim2 rotation=Y8 z=192.749*$in x=48.509*$in+2.5*$in
endif

#wired chambers
place fd  rename=WC1 rotation=Y16 width=7*$in height=6.5*$cm z=69.952*$in x=20.059*$in
place fd  rename=WC2 rotation=Y16 width=12*$in height=15*$cm z=137.200*$in x=39.341*$in
place fd  rename=WC3 width=12*$in height=15*$cm z=212.335*$in x=49.788*$in+2.5*$in
place fd  rename=WC4 width=16*$in height=15*$cm z=282.336*$in x=49.788*$in+30*$cm

#minerva
place fd  rename=MINERVA305 width=100*$cm height=100*$cm z=304.809*$in x=49.788*$in+30*$cm
place fd  rename=MINERVA325 width=100*$cm height=100*$cm z=324.809*$in x=49.788*$in+30*$cm
place fd  rename=MINERVA345 width=100*$cm height=100*$cm z=344.809*$in x=49.788*$in+30*$cm
place fd  rename=MINERVA365 width=100*$cm height=100*$cm z=364.809*$in x=49.788*$in+30*$cm
```

A.2 Root script template for reconstruction

- Input: g4beamline root file generated with the above code
- Output: data file with events reconstructed

```
{
for(int ttt=0; ttt!=1; ++ttt) { // for delayed trigger analysis (see ch.3)
  // parameters
  double TDelay = 25.0+ttt; // prefixed delay (ns)
  double TWidth = 100.0; // gate's width (ns)
  double xSigma =  0.5; // wirechamber resolution (mm)
  double tSigma = 0.15; // scintillator resolution (ns)

  TRandom3 rnd;
  double light  = 0.299792458; // (m/ns)
  //algorithm
  TChain *tr[6];
  for(int i=0; i!=6; ++i) TChain *tr[i]=new TChain();
  Float_t t, ev, id, ti, px, py, pz, x, y, z, sav[30];
  int     M[6];
  Float_t TID[2], X[5], Y[5], Z[5], T[2], eidTruth, tidTruth, pidTruth, pTruth, pRec, mRec;
  TFile *f;
  TNtuple *output=new TNtuple("rec", "rec", "eidTruth:tidTruth:pidTruth:pTruth:t1:mt1:x1:y1:z1:mx1:x2:y2:z2:
_____________________________________________mx2:x3:y3:z3:mx3:x4:y4:z4:mx4:t2:mt2:truth:pRec:mRec:x:y:z");
  for(int i=0; i!=1; ++i) {
    tr[0]->Add(Form("16GeV-QGSPBIC-50KE-%d-%d.root/VirtualDetector/ToF1;1",
                    i*300000+1,(i+1)*300000));
    tr[1]->Add(Form("16GeV-QGSPBIC-50KE-%d-%d.root/VirtualDetector/WC1;1",
                    i*300000+1,(i+1)*300000));
    tr[2]->Add(Form("16GeV-QGSPBIC-50KE-%d-%d.root/VirtualDetector/WC2;1",
                    i*300000+1,(i+1)*300000));
    tr[3]->Add(Form("16GeV-QGSPBIC-50KE-%d-%d.root/VirtualDetector/WC3;1",
                    i*300000+1,(i+1)*300000));
    tr[4]->Add(Form("16GeV-QGSPBIC-50KE-%d-%d.root/VirtualDetector/WC4;1",
                    i*300000+1,(i+1)*300000));
    tr[5]->Add(Form("16GeV-QGSPBIC-50KE-%d-%d.root/VirtualDetector/ToF2;1",
                    i*300000+1,(i+1)*300000));
  }
  for( int i=0; i!=6; ++i ) {
    tr[i]->SetBranchAddress("EventID",&ev); tr[i]->SetBranchAddress("Pz",&pz);
    tr[i]->SetBranchAddress("TrackID",&ti); tr[i]->SetBranchAddress("Px",&px);
    tr[i]->SetBranchAddress("PDGid",&id);   tr[i]->SetBranchAddress("Py",&py);
    tr[i]->SetBranchAddress("x",&x);        tr[i]->SetBranchAddress("y",&y);
    tr[i]->SetBranchAddress("z",&z);        tr[i]->SetBranchAddress("t",&t);
  }
  int it[6];
  for(int n=0; n!=6; ++n) it[n]=-1;
  for(;(it[5]+1)<tr[5]->GetEntries();) {
    tr[5]->GetEntry(++it[5]);
    if ((abs(id)==211)||(abs(id)==11)||(abs(id)==13)||(abs(id)==2212)) {
      for(int n=0; n!=6; ++n) M[n]=0;
      eidTruth=ev; T[1]=t; pidTruth=id; TID[1]=ti;
      X[4]=x; Y[4]=y; Z[4]=z;
      pTruth=sqrt(px*px+py*py+pz*pz);
      while ((ev==eidTruth)&&(it[5]<tr[5]->GetEntries())) {
        if ((abs(id)==11||abs(id)==211||abs(id)==2212||abs(id)==13)) {
          ++M[5];
          if (T[1]>TMath::Min(T[1],t)) {
            T[1]=t; pidTruth = id; TID[1]=ti;    pTruth=sqrt(px*px+py*py+pz*pz);
            X[4]=x; Y[4]=y; Z[4]=z;
          }
        }
        tr[5]->GetEntry(++it[5]);
      }
      --it[5]; T[0]=T[1];
      do {
        tr[0]->GetEntry(++it[0]);
      } while ((ev<eidTruth)&&(it[0]<tr[0]->GetEntries()));
```

```
64                      while ((ev==eidTruth)&&(it[0]<tr[0]->GetEntries())) {
          if ((abs(id)==11||abs(id)==211||abs(id)==2212||abs(id)==13)) {
            if ((((t+TDelay)>T[1])&&((t+TDelay)<(T[1]+TWidth)))||(((t+TWidth+TDelay)>T[1])&&((t+TDelay)<T[1]))){
              ++M[0];
              if (T[0]>TMath::Min(T[0],t)) {
                T[0]=t;
                TID[0]=ti;
              }
            }
          }
74        tr[0]->GetEntry(++it[0]);
        }
        --it[0];

        if (M[0]&&M[5]) {
          for(int wc=1; wc!=5; ++wc) {
            do {
              tr[wc]->GetEntry(++it[wc]);
            } while ((ev<eidTruth)&&(it[wc]<tr[wc]->GetEntries()));
                      while ((ev==eidTruth)&&(it[wc]<tr[wc]->GetEntries())) {
84          if ((abs(id)==11||abs(id)==211||abs(id)==2212||abs(id)==13)) {
              ++M[wc]; X[wc-1]=x; Y[wc-1]=y; Z[wc-1]=z;
            }
            tr[wc]->GetEntry(++it[wc]);
          }
          --it[wc];
        }
        sav[0]=eidTruth; sav[1]=TID[1]; sav[2]=pidTruth; sav[3]=pTruth;
        sav[4]=T[0];     sav[5]=M[0];   sav[6]=X[0];     sav[7]=Y[0];
        sav[8]=Z[0];     sav[9]=M[1];   sav[10]=X[1];    sav[11]=Y[1];
94      sav[12]=Z[1];    sav[13]=M[2];  sav[14]=X[2];    sav[15]=Y[2];
        sav[16]=Z[2];    sav[17]=M[3];  sav[18]=X[3];    sav[19]=Y[3];
        sav[20]=Z[3];    sav[21]=M[4];  sav[22]=T[1];    sav[23]=M[5];
        sav[24]=(TID[1]==TID[0]);
        // here is where p is reconstructed at first order
        // this line should be replaced by a function
        // that computes this better once B is measured
        for(int err=0; err!=4; ++err) {
          X[err]+=rnd.Gaus(0,xSigma); Z[err]+=rnd.Gaus(0,xSigma);
        }
104     sav[25]=-102.0/(atan((X[3]-X[2])/(Z[3]-Z[2]))-atan((X[1]-X[0])/(Z[1]-Z[0])));
        // here is where m is reconstructed at first order
        Float_t PathS=0;
        PathS+=9.5/7*sqrt((X[0]-X[1])*(X[0]-X[1])+(Y[0]-Y[1])*(Y[0]-Y[1])+(Z[0]-Z[1])*(Z[0]-Z[1]));
        PathS+=sqrt((X[1]-X[2])*(X[1]-X[2])+(Y[1]-Y[2])*(Y[1]-Y[2])+(Z[1]-Z[2])*(Z[1]-Z[2]));
        PathS+=9.5/7*sqrt((X[2]-X[3])*(X[2]-X[3])+(Y[2]-Y[3])*(Y[2]-Y[3])+(Z[2]-Z[3])*(Z[2]-Z[3]));
        PathS=0.92*PathS/1000.0; // convenient factor
        T[0]+=rnd.Gaus(0,tSigma); T[1]+=rnd.Gaus(0,tSigma);
        sav[26]=(T[1]-T[0]);
        sav[26]=sav[25]*sqrt(light*sav[26]*light*sav[26]-PathS*PathS)/PathS;
114     sav[27]=X[4]; sav[28]=Y[4]; sav[29]=Z[4];
        output->Fill(sav);
      }
    }
  }
  cout << "TDelay " << TDelay << " | TWidth " << TWidth << endl;
  cout << "e- e+    | " << output->GetEntries("truth&&mx1==1&&mx2==1&&mx3==1&&mx4==1&&abs(pidTruth)==11")
       << endl;
  cout << "pi- pi+  | " << output->GetEntries("truth&&mx1==1&&mx2==1&&mx3==1&&mx4==1&&abs(pidTruth)==211")
       << endl;
124 cout << "mu- mu+  | " << output->GetEntries("truth&&mx1==1&&mx2==1&&mx3==1&&mx4==1&&abs(pidTruth)==13")
       << endl;
  cout << "protons  | " << output->GetEntries("truth&&mx1==1&&mx2==1&&mx3==1&&mx4==1&&abs(pidTruth)==2212")
       << endl;
  cout << "total    | " << output->GetEntries("truth&&mx1==1&&mx2==1&&mx3==1&&mx4==1") << endl;
}
TGraph *graph;
if (1) {
  TCanvas *c1=new TCanvas("c1", "c1");
  c1->SetFillColor(kWhite); c1->SetFrameFillColor(kWhite);
134 c1->SetGridx(1); c1->SetGridy(1);
  output->Draw("pidTruth:mRec","mx1==1&&mx2==1&&mx3==1&&mx4==1&&mt1==1&&mt2==1");
```

```
    TGraph *tmp=c1->FindObject("Graph");
    tmp->SetName("Graphs");
    graph=(TGraph*) tmp->Clone();
    graph->SetTitle("");
    graph->GetXaxis()->SetTitle("Reconstructed Mass [MeV/c2]");
    graph->GetYaxis()->SetTitle("Truth PDGid");
    graph->SetMarkerStyle(4);
    graph->Draw("AP");
144 }
    if (0) {
    TCanvas *c1=new TCanvas("c1", "c1");
    c1->SetFillColor(kWhite); c1->SetFrameFillColor(kWhite);
    c1->SetGridx(1); c1->SetGridy(1);

    output->Draw("pTruth:pRec","mx1==1&&mx2==1&&mx3==1&&mx4==1&&mt1==1&&mt2==1&&(abs(pidTruth)==211||
    ______________________________abs(pidTruth)==13)");
    tmp=(TGraph*)c1->FindObject("Graph");
    tmp->SetName("GraphsPi");
154 TGraph *graphPi=(TGraph*) tmp->Clone();

    output->Draw("pTruth:pRec","mx1==1&&mx2==1&&mx3==1&&mx4==1&&mt1==1&&mt2==1&&abs(pidTruth)==11");
    TGraph *tmp=(TGraph*)c1->FindObject("Graph");
    tmp->SetName("GraphsE");
    TGraph *graphE=(TGraph*) tmp->Clone();

    output->Draw("pTruth:pRec","mx1==1&&mx2==1&&mx3==1&&mx4==1&&mt1==1&&mt2==1&&abs(pidTruth)==2212");
    TGraph *tmp=(TGraph*)c1->FindObject("Graph");
    tmp->SetName("GraphsP");
164 TGraph *graphP=(TGraph*) tmp->Clone();

    graphPi->SetTitle("");
    graphPi->GetXaxis()->SetTitle("Reconstructed Momentum [MeV/c]");
    graphPi->GetXaxis()->SetRangeUser(200,1500);
    graphPi->GetYaxis()->SetRangeUser(200,1500);
    graphPi->GetYaxis()->SetTitle("Truth Momentum [MeV/c]");
    graphPi->SetMarkerStyle(7); graphPi->SetMarkerColor(kBlue-3);
    graphP->SetMarkerStyle(22); graphP->SetMarkerColor(kRed-3);
    graphE->SetMarkerStyle(20); graphE->SetMarkerColor(kGreen-3);
174 graphPi->Draw("AP");
    graphP->Draw("PS");
    graphE->Draw("PS");
    }
    }
```

Bibliography

[1] C. Amsler et al. Review of particle physics. *Physics Letters B*, 667:1, July 2008.

[2] W.S.C. Williams. *An Introduction to Elementary Particle Physics*. Academic Press, 1971.

[3] W. R. Leo. *Techniques for Nuclear and Particle Physics Experiments*. Springer-Verlag, 1994.

[4] C. Grupen and B. A. Shwartz. *Particle Detectors*. Cambridge University Press, 2008.

[5] W.H. Barkas and M.J. Berger. Tables of energy losses and ranges of heavy charged particles. Technical report, NASA-SP, 1964.

[6] P. Adamson et al. Minos technical design report. Technical report, MINOS Collaboration, 2009.

[7] P. Adamson et al. Nova technical design report. Technical report, NOVA Collaboration, 2009.

[8] C Quigg. *Gauge Theories of the Strong, Weak, and Electromacnetic Interactions*. Westview Press, 1999.

[9] P. Adamson et al. Minerνa technical design report. Technical report, MINERvA Collaboration, 2008.

[10] Klaus Winter. *Neutrino Physics*. Cambridge University Press, 2000.

[11] Fermilab. Proton driver. http://protondriver.fnal.gov/.

[12] 621.384.SCH. *Particle accelerators and their uses*. IDonKnow, IDK.

[13] Fermilab. Booster. http://www-ad.fnal.gov/proton/booster/booster.html.

[14] Fermilab. Meson test facility. http://www-ppd.fnal.gov/MTBF-w/.

[15] C. Pérez et al. Minerva testbeam beamline design. In *Hadron Collider Physics Symposium 2008 Proceedings*, 2005.

[16] CERN. Geant4: Toolkit for simulation of particles through matter, June 2008.

[17] T. Roberts. G4beamline, June 2008.

[18] D. Jansen. Private Communication, June 2008.

[19] 539.1.043.HOL. *Handbook of Radiation Effects*. IdonwKnow, IDK.

[20] Fermilab. Accelerator division, September 2008.

[21] R.A. Burnstein et al. Hypercp: A high-rate spectrometer for the study of charged hyperon and kaon decays. *Nuclear Instruments and Methods in Physics Research A*, 541:516–565, 2005.

[22] J. Jackson. *Classical Electrodynamics, 3rd Ed.* Jhon Wiley and Sons, 1999.

[23] C. Pérez, R. Gran, et al. Mtest tertiary beam target and collimator commissioning analysis. Technical report, MINERvA Collaboration, 2009.

[24] Fermilab. Es&h section. http://www-esh.fnal.gov/pls/default/esh_home_page.html.

[25] C. Araujo. *Investigación y Calibración del Sistema de Tiempo de Vuelo del Test de Prueba del Experimento MINERνA*. PhD thesis, Pontificia Universidad Católica del Perú, 2009.

[26] MINERνA Collaboration. Minerνa logbook, September 2008.

[27] R. Gran. Private Communication, December 2008.